Vol. 104 Nº1 Enero-Junio 2017 ISSN 2545-8655

ANALES DE LA ASOCIACIÓN QUÍMICA ARGENTINA

THE JOURNAL

OF THE

ARGENTINE CHEMICAL SOCIETY

Anales de la Asociación Química Argentina

The Journal of the Argentine Chemical Society

Editada desde 1913

e-mail: anales.aqa@gmail.com

Intellectual property registry No. 164.756

Asociación Química Argentina
Sánchez de Bustamante 1749, 1425 Buenos Aires, Argentina
TE/FAX: 54-11-4822-4886
http://www.aqa.org.ar

Contenido

Vol. 104 Nº1, Enero-Junio 2017

Editorial pp. *i*

Three New Thiosaccharin Derivatives Generated in a Complex Reaction System pp. 1 - 10
Gustavo A. Echeverría, Oscar E. Piro, Juan Zinczuk and Enrique J. Baran

Kinetics of Water Sorption and Sugar Crystallization in Freeze-dried Bananas Previously Immersed in Concentrated Sucrose and Trehalose Solution pp. 11-20
Hector Iglesias, Mara V. Galmarini, Luis F. Díaz and J. Chirife

Sustainable Biodiesel: Kinetic Study and Modeling of Catalytic Esterification of Used Vegetable Oils as the First Stage of the Product Process pp. 21-33
Verónica Rodríguez, María F. Laborde, María C. Gely and Ana M. Pagano

Density Functional Theory (DFT) Study of H_2S Interactions on the P_r-doped $C_eO_2(111)$ Surface pp. 34-43
Alejandro Kinbaum, Eduardo Poggio-Fraccari, Fernando Mariño and Beatriz Irigoyen

Nickel Deposition on Ceria: a DFT+U Study pp. 44-53
Dan Rajsfus, Agustín Salcedo, Brian Milberg and Beatriz Irigoyen

EDITORIAL

En este nuevo número de Anales de la Asociación Química Argentina, cuya edición hemos retomado, quisiera destacar la importancia de esta publicación para muchas generaciones de químicos. En tiempos que parecen muy lejanos, pero en la historia no lo son tanto, las comunicaciones no eran lo que hoy día, y tener una revista de la calidad de Anales representaba estar informado de las actividades de investigación en Química en Argentina y países vecinos.

La Química es una ciencia básica, central para mejorar la calidad de vida de la población, ya que es el eje de estudios fundamentales y estratégicos para el desarrollo, tales como garantizar agua y alimentos seguros a la sociedad. El año 2011 fue declarado el año internacional de la Química por conmemorarse los cien años del Premio Nobel de Química a Madame Curie. El lema fue: Química, nuestra vida, nuestro futuro.

La Asociación Química Argentina, con 105 años de vida, es la Asociación que nuclea a todos los químicos independiente de su orientación, tanto de la Academia como de la Industria. Permite un espacio donde podamos nuclearnos y coincidir, creando sinergias a partir del intercambio. En todos estos años ha mantenido la periodicidad de los Congresos Nacionales, que brindan el marco para el encuentro, para conocernos, para compartir.

Anales de la Asociación Química Argentina constituye un medio de comunicación esencial para plasmar los avances de la Química en nuestro país y es importante que recupere el protagonismo que supo tener en el ámbito local.

Dra. Alicia Fernández Cirelli

Presidente

Asociación Química Argentina

Journal of the Argentine Chemical Society

THREE NEW THIOSACCHARIN DERIVATIVES GENERATED IN A COMPLEX REACTION SYSTEM

Gustavo A. Echeverría [1], Oscar E. Piro [1], Juan Zinczuk [2] and Enrique J. Baran [3,*]

[1] *Dto. de Física and IFLP (CONICET), Fac. de C.s Exactas, UNLP, 1900 La Plata, Argentina.*

[2] *IQUIR, CONICET/UNR, Fac. de Cs. Bioquímicas y Farmacéuticas, UNR, 2000 Rosario, Argentina.*

[3] *CEQUINOR, CONICET/UNLP, Fac. de Cs. Exactas, UNLP, 1900 La Plata, Argentina.*

[*] Corresponding author: baran@quimica.unlp.edu.ar

Received August 2nd, 2012. Accepted, September 10th, 2012.

Resumen

La reacción entre tiosacarina y etilamina muestra ser relativamente compleja. El producto principal de esta reacción es el 1,1 dióxido de 3-etilamino-1,2 benzisotiazol (**1**), que pudo ser claramente identificado por espectroscopia NMR e IR. El tiosacarinato de etilamonio (**2**) y el 1,1 dióxido de 3-vinilamino-1,2 benzisotiazol (**3**) se generan como subproductos minoritarios de la reacción y sus estructuras pudieron ser determinadas por métodos de difracción de rayos X. La sal (**2**) cristaliza en el sistema monoclínico, grupo espacial $P2_1/c$ con a=13.1367(5), b=9.9721(4), c=8.8217(3) Å, β=99.125(4)°, y Z=4, mientras que el compuesto (**3**) pertenece al grupo espacial $P2_1/m$ con a=7.1572(5), b=7.0242(7), c=9.5503(8) Å, β=95.008(7)°, y Z=2.

Abstract

The reaction between thiosaccharin and ethylamine showed to be relatively complex. The main product of this reaction is 3-ethylamino-1,2-benzisothiazole 1,1-dioxide (**1**), which could be clearly identified by NMR and IR spectroscopies. Ethylammonium thiosaccharinate (**2**) and 3-vinylamino-1,2-benzisothiazole 1,1 dioxide (**3**) were generated as minor by products during this reaction and their structures were determined by X-ray diffraction methods. The (**2**) salt crystallizes in the monoclinic $P2_1/c$ space group with a=13.1367(5), b=9.9721(4), c=8.8217(3) Å, β=99.125(4)°, and Z=4, whereas compound (**3**) belongs to the $P2_1/m$ space group with a=7.1572(5), b=7.0242(7), c=9.5503(8) Å, β=95.008(7)°, and Z=2.

Palabras clave: *Reacción tiosacarina/etilamina; 1,1 dióxido de 3-etilamino-1,2-benzisotiazol; tiosacarinato de etilamonio; 1,1 dióxido de 3-vinilamino-1,2-benzisotiazol; estructuras cristalinas*

Keywords: *Thiosaccharin/ethylamine reaction; 3-ethylamino-1,2-benzisothiazole 1,1 dioxide; ethylammonium thiosaccharinate; 3-vinylamino-1,2-benzisothiazole 1,1 dioxide; crystal structures.*

1. Introduction

Recently, we have prepared two simple salts derived from thiosaccharin, 1-2-benzisothiazol-3-(2H)-thione-1,1-dioxide, namely hexamethylenediammonium bis(thiosaccharinate) dihydrate [1] and pyridinium thiosaccharinate thiosaccharin [2]. As an extension of this work we have now attempted to prepare a similar salt derived from ethylamine, following a similar procedure as that described for the preparation of the analogous saccharinate salt, ethylammonium saccharinate [3]. Notwithstanding, the reaction between thiosaccharin and ethylamine showed a greater complexity than those with saccharin, allowing the identification of three new compounds, two of which could be characterized by structural single crystal X-ray diffraction methods.

2. Materials and Methods

Synthesis of the compounds

Thiosaccharin was obtained by heating a mixture of 0.1 mol of saccharin (Aldrich 99%) and 0.11 mol of P_2S_5 (Merck) under a N_2 atmosphere, according to the procedure described by Meadow and Cavagnol [4]. The reaction mixture was extracted with benzene, and the crude orange-yellow product was recrystallized from this solvent. Its purity was confirmed by a sharp melting point (181-182°C) and by its IR and Raman spectra [5].

In order to attempt the preparation of ethylammonium thiosaccharinate, the same procedure as described by Wang *et al.* [3] for the synthesis of ethylammonium saccharinate was employed, i.e. 1 mmol of thiosaccharin were dissolved in 15 mL of ethylamine (Carlo Erba) and the mixture was stirred during 20 minutes at room temperature and then left in air. After evaporation of the solvent a yellow powder was obtained. This powder was then recrystallized twice from methanol. The observation of the product under a microscope revealed that the bulk material was conformed mainly by a yellow powder and only a few very small and not well-formed single crystals. The bulk yellow mass was characterized by FTIR and NMR spectroscopy while the X-ray diffraction study of the isolated crystals showed the presence of two other different products, one of which was the expected ethylammonium thiosaccharinate.

Spectroscopic measurements

The infrared spectra of the bulk material were recorded on a Bruker EQUINOX-55 Fourier transform infrared spectroscopy (FTIR) instrument, using the KBr pellet technique.

NMR spectra were recorded in DMSO-d_6 using a Bruker Avance 300 instrument. Chemical shifts are reported in ppm downfield from tetramethylsilane. ^{1}H-spectra were recorded at 300 MHz and ^{13}C-spectra at 75 MHz.

Crystal structure determinations

The measurements for the other two compounds were performed on an Oxford Xcalibur, Eos, Gemini CCD diffractometer with graphite-monochromatized CuKα (λ=1.54178Å) radiation. X-ray diffraction intensities were collected (ω scans with ϑ and κ-offsets), integrated and scaled with the CRYSALISPRO [6] suite of programs. The unit cell parameters were obtained by least-squares refinement based on the angular settings for all collected reflections with intensities larger than seven times the standard deviation of measurement errors, using CRYSALISPRO. Data were corrected empirically for absorption employing the multi-scan method implemented in CRYSALISPRO. The structure was solved by direct methods with SHELXS-97 [7] and the molecular model refined by a full-matrix least-squares procedure on F^2 with SHELXL-97 [8]. Hydrogen atoms were located stereo-chemically and refined with the riding model. The methyl and ammonium H-positions in the $[CH_3\text{-}CH_2\text{-}NH_3]^+$ cation of $EtNH_3$(tsac) were optimized by treating them as rigid groups which were allowed to rotate during the refinement around the corresponding C-C or N-C bonds. As a result, both CH_3 and NH_3^+ groups converged to staggered conformations.

Crystal data and structure refinement results are summarized in Table 1.

Tables containing complete information on fractional atomic coordinates and equivalent isotropic displacement parameters of the non-H atoms, atomic anisotropic displacement parameters, and hydrogen atom positions have been deposited at the Cambridge Crystallographic Data Centre, under deposition numbers CCDC 868705 (ethylammonium thiosaccharinate, **2**) and CCDC 868706 (3-vinylamino-1,2-benzisothiazole 1,1 dioxide, **3**).

3. Results and Discussion

The reaction between thiosaccharin and ethylamine seems to be relatively complex, as mentioned in the introduction. The main product of this reaction is generated in the form of a yellow powder and could be characterized as 3-ethylamino-1,2-benzisothiazole 1,1-dioxide (**1**). The other two products, apparently present as traces, were identified as ethylammonium thiosaccharinate (**2**) and 3-vinylamino-1,2-benzisothiazole 1,1-dioxide (**3**).

Table 1. Crystallographic data and structure refinement details for ethylammonium thiosaccharinate (**2**), and 3-vinylamino-1,2-benzisothiazole 1,1 dioxide (**3**).

Compound	(2)	(3)
Empirical formula	$C_9H_{12}N_2O_2S_2$	$C_9H_8N_2O_2S$
Formula weight	244.33	208.23
Temperature, K	295(2)	295(2)
Crystal system	monoclinic	monoclinic
Space group	$P2_1/c$	$P2_1/m$
a, Å	13.1367(5)	7.1572(5)
b, Å	9.9721(4)	7.0242(7)
c, Å	8.8217(3)	9.5503(8)
β, deg	99.125(4)	95.008(7)
V, Å^3	1141.02(7)	478.30(7)
D_c, gcm^{-3}	1.42	1.44
Z	4	2
Crystal size, mm^3	0.42 x 0.25 x 0.08	0.31 x 0.25 x 0.05
Absorption coefficient, mm^{-1}	4.105	2.818
F(000)	512	216
θ range for data collection, deg	3.41 - 70.99	4.65 - 70.98
Index ranges	-16 ≤h≤16, -10≤k≤12, -10≤l≤8	-8 ≤h≤7, -6≤k≤8, -11≤l≤11
Reflections collected	7327	2516
Independent reflections/R_{int}	2208/0.0313	1005/0.0258
Observed reflections [$I \geq 2\sigma(I)$]	1942	846
Data/restraints/parameters	2208/ 0 /138	1005/ 0 / 82
Goodness-of-fit on F^2	1.053	1.052
Final índices R1/wR2 [$I \geq 2\sigma(I)$]	0.0371 / 0.1043	0.0531 / 0.1461
Final índices R1/wR2 (all data)	0.0422 / 0.1108	0.0615 / 0.1581
Largest diff. peak/hole, eÅ^{-3}	0.311 / -0.307	0.330 / -0.360

The formation of the bulk product (**1**) occurs by direct reaction between thiosaccharin and ethylamine, with liberation of SH_2, and with the intermediate generation of (**2**) as depicted in Figure 1.

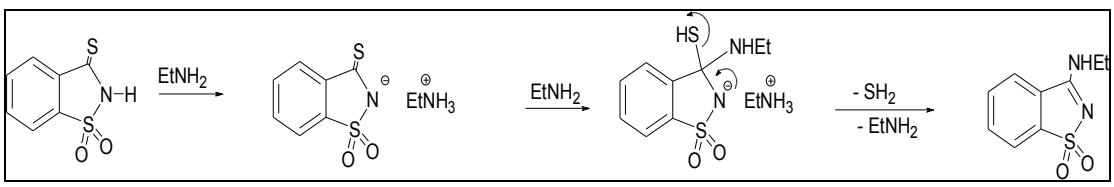

Figure 1. Reaction schema for the formation of the main product of the reaction between thiosaccharin and ethylamine, 3-ethylamino-1,2-benzisothiazole 1,1 dioxide (**1**).

The generation of this product could be unambiguously confirmed by NMR and IR spectroscopies, as shown in Tables 2 and 3. These spectra are clearly compatible with the presence of this molecule, as shown by the presented data, analyzed on the basis of some standard references [9-11] and in the case of the IR spectrum also by comparison with the data of thiosaccharin [5].

Table 2. NMR analysis of 3- ethylamino-1,2-benzisothiazole 1,1-dioxide (**1**)

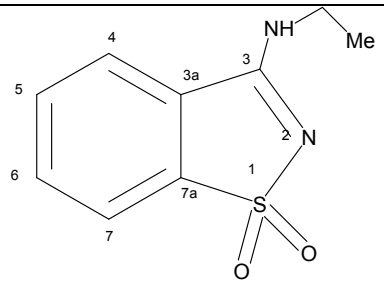

^{1}H NMR 300 MHz (DMSO-d_6)

δ_H = 1.11 (t, J= 7.2Hz, 3H, Me), 2.80 (m, 2H, CH_2) 7.60 (m, 2H, H_5, H_6), 7.64 (ddd, J= 1.7, 2.1, 6.3 Hz, 1 H, H_4), 7.90 (dd, J = 2.1, 6.3 Hz, 1 H, H_7)

^{13}C NMR 75 MHz (DMSO-d_6)

δ_C = 12.97 (Me), 34.74 (CH_2), 119.42 (C_4), 125.52 (C_7), 131.31 (C^*_6), 132.54 (C^*_5), 137.00 (C_{3a}), 138.32 (C_{7a}), 154.0 (C3)

Values of C* may be interchanged.

Spectral structure: dd: double doublet; ddd: double double doublet; t: triplet; m: multiplet.

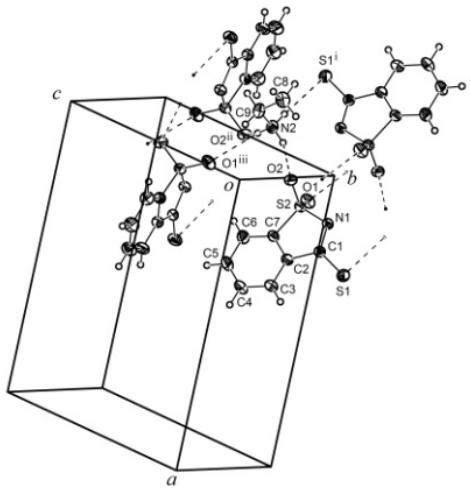

Figure 2. View of ethylammonium thiosacharinate (**2**), showing the labeling of the non-H atoms and their displacement ellipsoids at the 30% probability level. H-bonds are indicated by dashed lines. The symmetry operations used to generate equivalent atoms are i) -x, -y+2, -z, ii) -x, y-1/2, -z+1/2 and iii) x, -y+3/2, z+1/2.

Table 3. Assignment of the most characteristic IR bands of 3- ethylamino-1, 2-benzisothiazole 1,1-dioxide (**1**)

Band position (cm^{-1})	Approximate assignment
3234 vs	ν(NH)
3008 m, 2882 m	$\nu(CH_3)$
1594 vs	$\nu_{CC} + \delta_{PhH} + \delta_{CCC}$
1454 s	$\delta_{as}(CH_3) + \delta_{sciss}(CH_2) + \nu_{CC}$
1343 vs	$\nu_{as}(SO_2)$
1261 vs, 1234 s	$\nu_{CC} + \nu_{NC(ring)}$
1194 m	$\nu_{NC(amino)}$
1142 vs, 1115 vs	$\nu_s(SO_2) + \nu_{CC} + \delta_{PhH}$
774 vs	δ_{CCC}
754 m	δ_{wagg}(NH)
774 vs	δ_{CCC}
593 vs	$\delta(SO_2) + \delta_{CCC}$

vs: very strong; s: strong; m; medium

The two minor byproducts of the main reaction, (**2**) and (**3**), could be identified by single crystal X-ray diffraction. Figure 2 shows the ORTEP [12] drawing of ethylammonium thiosaccharinate (**2**). Corresponding bond distances and angles are presented in Table 4.

Table 4. Bond lengths (Å) and angles (deg) for (**2**)

C(1)-N(1)	1.337(2)	C(5)-C(6)	1.393(3)
C(1)-C(2)	1.499(3)	C(6)-C(7)	1.382(3)
C(1)-S(1)	1.671(2)	C(7)-S(2)	1.759(2)
C(2)-C(7)	1.379(3)	C(8)-C(9)	1.493(3)
C(2)-C(3)	1.384(3)	C(9)-N(2)	1.472(3)
C(3)-C(4)	1.388(4)	N(1)-S(2)	1.620(2)
C(4)-C(5)	1.372(4)	O(1)-S(2)	1.438(2)
		O(2)-S(2)	1.444(2)
N(1)-C(1)-C(2)	113.4(2)	C(2)-C(7)-S(2)	106.8(1)
N(1)-C(1)-S(1)	123.4(2)	C(6)-C(7)-S(2)	129.9(2)
C(2)-C(1)-S(1)	123.3(1)	N(2)-C(9)-C(8)	111.7(2)
C(7)-C(2)-C(3)	119.8(2)	C(1)-N(1)-S(2)	111.5(1)
C(7)-C(2)-C(1)	111.3(2)	O(1)-S(2)-O(2)	114.4(1)
C(3)-C(2)-C(1)	128.9(2)	O(1)-S(2)-N(1)	111.5(1)
C(2)-C(3)-C(4)	117.9(2)	O(2)-S(2)-N(1)	110.17(9)
C(5)-C(4)-C(3)	121.4(2)	O(1)-S(2)-C(7)	111.96(9)
C(4)-C(5)-C(6)	121.6(2)	O(2)-S(2)-C(7)	110.59(9)
C(7)-C(6)-C(5)	116.0(2)	N(1)-S(2)-C(7)	96.92(9)
C(2)-C(7)-C(6)	123.3(2)		

As expected, the thiosaccharinate $C_7H_4NO_2S_2^-$ molecular skeleton is planar (*rms* distance of atoms from the least-squares plane of 0.0158 Å). By comparing with the neutral thiosaccharin

(Htsac) molecule [13], it can be appreciated that the major bonding changes in the charged moiety occur at the thioamidic functional group. In fact, upon deprotonation, the excess nitrogen electron mainly contributes to a delocalized C(1)-N(1)-S(2) bonding. This is shown by the shortening observed in both the N(1)-C(1) bond length [from 1.384 Å in Htsac to 1.337(2) Å in $tsac^-$] and the N(1)-S(2) distance [from 1.664 Å to 1.620(2) Å], and also by the lengthening of the C(1)-S(1) bond [from 1.622 Å in Htsac to 1.671(2) Å in $tsac^-$]. Our bond distances and angles agree well with those reported for the hexamethylenediammonium, sodium, potassium, ammonium, and bis(triphenylphosphine) iminium thiosaccharinate salts [1,13-17].

The crystal is further stabilized by the extensive 3-D net of H-bonds (see Figure 2). The H-bonding structure involves as donor the ethylammonium NH_3^+ groups and as acceptors the amidic nitrogen, both sulfonyl oxygens and the exocyclic sulfur atom of neighboring thiosaccharinate molecules. A detail of the H-bonding structure is given in Table 5.

Table 5. Hydrogen bonds for (**2**)

D-H	d(D-H)	d(H···A)	<D-H··· A	d(D··A)	A	Symmetry operation
N2-H2A	0.890	2.522	163.91	3-387	S1	[-x, -y+2, -z]
N2-H2B	0.890	2.385	140.35	3.122	O2	[-x, y-1/2, -z+1/2]
N2-H2B	0.890	2.533	132.91	3.206	O1	[x, -y+3/2, z+1/2]
N2-H2C	0.890	2.213	150.98	3.022	O2	

In the case of 3-vinylamino-1,2-benzisothiazole 1,1-dioxide (**3**), the molecule lies on a crystallographic mirror plane. It is a thiosaccharin derivative where the sulfur atom is replaced by the vinylamino cation, $-(NH^+)-CH)=CH_2$, as shown in Figure 3.

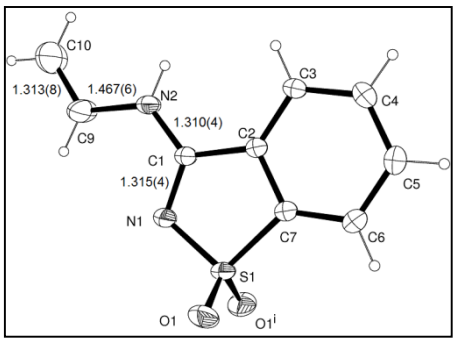

Figure 3. View of 3-vinylamino-1,2-benzisothiazole 1,1-dioxide (**3**). F convenience, the figure includes a few selected bond distances (in Å).

Because the excess electron at the heterocyclic nitrogen, it is expected that the molecule possesses a large dipole moment contribution (of about 3 D) nearly parallel to the hetero-cycle

axis due to this charge separation. Bond distances and angles for this molecule are shown in Table 6.

Table 6. Bond lengths (Å) and angles (deg) for (**3**)

C(1)-N(2)	1.310(4)	C(5)-C(6)	1.397(6)
C(1)-N(1)	1.315(4)	C(6)-C(7)	1.380(5)
C(1)-C(2)	1.487(5)	C(7)-S(1)	1.761(4)
C(2)-C(7)	1.376(4)	C(9)-C(10)	1.313(8)
C(2)-C(3)	1.387(4)	C(9)-N(2)	1.467(6)
C(3)-C(4)	1.387(5)	N(1)-S(1)	1.615(3)
C(4)-C(5)	1.380(6)	O(1)-S(1)	1.424(2)
N(2)-C(1)-N(1)	122.4(3)	C(2)-C(7)-C(6)	123.2(3)
N(2)-C(1)-C(2)	121.7(3)	C(2)-C(7)-S(1)	107.0(3)
N(1)-C(1)-C(2)	115.9(3)	C(6)-C(7)-S(1)	129.8(3)
C(7)-C(2)-C(3)	119.9(3)	C(10)-C(9)-N(2)	118.1(5)
C(7)-C(2)-C(1)	109.8(3)	C(1)-N(1)-S(1)	110.3(3)
C(3)-C(2)-C(1)	130.3(3)	C(1)-N(2)-C(9)	123.7(3)
C(2)-C(3)-C(4)	117.7(3)	O(1')-S(1)-O(1)	114.05(19)
C(5)-C(4)-C(3)	121.9(4)	O(1)-S(1)-N(1)	110.85(11)
C(4)-C(5)-C(6)	120.6(4)	O(1)-S(1)-C(7)	111.42(11)
C(7)-C(6)-C(5)	116.6(3)	N(1)-S(1)-C(7)	97.01(15)

O(1') is related to O(1) by the crystallographic reflection operation x, -y+1/2, z

By comparison with the thiosaccharinate anion in (**2**), a significant bond shortening (0.023 Å) in the C1-N1 bond length [from 1.337(2) in $tsac^-$ to 1.315(4) Å in (**3**)] is observed. This, in conjunction with an equal C1-N2 distance [1.310 Å] on the pendant arm, indicates a substantial N2-C1-N1 π-bonding delocalization, generating partial double bonds. The short C9-C10 distance observed of 1.313(8) Å confirms the double bond character of this link and hence the identification of the terminal $-(CH)=CH_2$ vinyl group.

Neighboring molecules related by a lattice translation along the crystal *a*-axis are linked to each other by bifurcated N-H+…O bonds [d(N…O) = 3.315 Å and ∠(N-H…O) = 148.5°], hence giving rise to a polymeric structure that extends along that axis. This is further stabilized by intra-chain dipole-dipole interaction, as the molecular dipoles are parallel to each other and nearly along the polymer. Neighboring polymers in the lattice, symmetry related to each other through the two-fold screw-axis along *b*, are hold by both inter-chain dipole-dipole attraction, as they run in opposite directions, and van der Waals interaction between the stacked planar molecules (*b*/2= 3.51 Å apart), as shown in Figure 4.

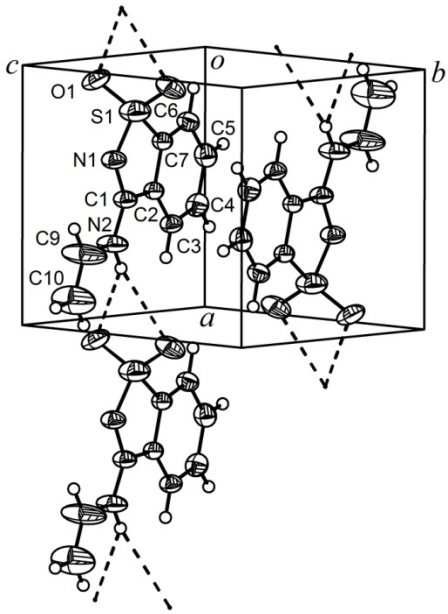

Figure 4. View of (**3**) showing the polymeric arrangement of molecules extending along the crystal *a-axis*. An unlabeled monomeric unit of a neighboring polymer in the lattice is also shown.

Finally, the comparison of the two solved structures clearly emphasizes the bonding versatility of the N-atom in this type of relatively simple molecular arrangements.

5. Conclusions

The reaction between thiosaccharin and ethylamine is much more complex than the similar reaction with saccharin, in which only ethylammonium saccharinate is obtained in a direct and straightforward way. On the contrary, in the case of the reaction with thiosaccharin, the main product generated is 3-ethylamino-1,2-benzisothiazole 1,1-dioxide, which could be unambiguously characterized by infrared and NMR (^{1}H and ^{12}C) spectroscopies. Two other products, present as traces in the reaction mixture, were identified as 3-vinylamino-1,2-benzisothiazole 1,1-dioxide and the expected ethylammonium thiosaccharinate, and were fully characterized by single crystal X-ray diffractometry. The first one crystallizes in the monoclinic $P2_1/m$ space group with Z = 2 and presents a polymeric arrangement along the *a* crystal axis, stabilized by hydrogen bonds and intra-chain dipole-dipole interactions. Ethylammonium thiosaccharinate crystallizes in the also monoclinic space group $P2_1/c$ with Z = 4 and its structure is stabilized by an extensive 3-D net of hydrogen bonds.

Acknowledgements: This work was supported by the Universidad Nacional de La Plata, by CONICET (PIP 1529), and by ANPCyT (PME06 2804 and PICT06 2315) of Argentina. G.A.E, O.E.P and J.Z. are members of the Research Career from CONICET.

References

[1] E. J. Baran, O. E. Piro, J. Zinczuk, *Z. Naturforsch.* 62b (2007) 1530-1534.

[2] O. E. Piro, J. Zinczuk, E .J. Baran, *Z. Naturforsch.* 63b (2008) 877-879.

[3] Z. L. Wang, L. H. Wei, M. X. Li, J.P. Wang, *Acta Crystallogr.* E62 (2006) o1800-o1801.

[4] J. R. Meadow, J.C Cavagnol, *J. Org. Chem.* 16 (1951) 1582-1587.

[5] E. J. Baran, J. Zinczuk, *J. Raman Spectr. 37* (2006) 948-950.

[6] CRYSALISPRO, Oxford Diffraction Ltd., version 1.171.33.48 (release15-09-2009 CRYSALIS 171.NET)

[7] G. M. Sheldrick, SHELXS-97, *Program for crystal structure resolution*, University of Göttingen, Göttingen (Germany), 1997.

[8] G.M. Sheldrick, SHELXL-97, *Program for crystal structure analysis*, University of Göttingen, Göttingen (Germany), 1997.

[9] B. Breitmaier, *Structure Elucidation by NMR in Organic Chemistry*, J. Wiley, Chichester, 1993.

[10] D. Lin-Vien, N. B. Colthup, W.G. Fateley, J.G. Grasselli, *The Handbook of Infrared and Raman Characteristic Frequencies of Organic Molecules*, Academic Press, Boston, 1991.

[11] B. Smith, *Infrared Spectral Interpretation*, CRC Press, Boca Raton, 1999.

[12] C.K. Johnson, *ORTEP-II, A Fortran thermal ellipsoid program*, Report ORNL-5318, Oak Ridge National Laboratory, Oak Ridge, TN (USA), 1976.

[13] O. Grupce, M. Penavic, G. Jovanovski, *J. Chem. Crystallogr. 24* (1994) 581-586.

[14] M. Penavic, G. Jovanovski, O. Grupce, *Acta Crystallogr. C46* (1990) 2341-2344.

[15] M. Penavic, O. Grupce, J. Jovanovski, *Acta Crystallogr. C47* (1991) 1821-1823.

[16] E.J. Baran, O.E. Piro, J. Zinczuk, *Z. Anorg. Allg. Chem. 632* (2006) 437-440.

[17] M. Dennehy, O.V. Quinzani, S.D. Mandolesi, J.A Guida. G.A. Echeverría, O.E. Piro, *Monatsh. Chem. 138* (2007) 669-675.

Journal of the Argentine Chemical Society

KINETICS OF WATER SORPTION AND SUGAR CRYSTALLIZATION IN FREEZE-DRIED BANANAS PREVIOUSLY IMMERSED IN CONCENTRATED SUCROSE AND TREHALOSE SOLUTION

Hector Iglesias[1], Mara V. Galmarini,[2,3*], Luis F. Díaz Barrios[1] and J. Chirife[3]

[1] *Dto. de Industrias, Facultad de Ciencias Exactas y Naturales, UBA; CABA, Argentina.*
[2] *Member of CONICET Godoy Cruz 2290 (C1425FQB) CABA, Argentina.*
[3] *Facultad de Ingeniería y Ciencias Agrarias, Pont. U. Católica Argentina., CABA, Argentina.*
**Corresponding author: mgalmarini@gmail.com*

Received October 31st, 2016. Accepted in final form,March 6th, 2017

Resumen

Se deshidrataron osmóticamente rodajas de banana, utilizando soluciones de 45% p/p de sacarosa o trehalosa. Luego fueron liofilizadas a una actividad de agua (a_w) de aproximadamente 0,10. Los productos liofilizados se almacenaron a diferentes humedades relativas (%HR) durante 100 días para detectar la pérdida de humedad asociada a la cristalización del azúcar. Después de una absorción inicial de agua, no se observó pérdida de contenido de humedad absorbida en función de %HR, probablemente debido a la cristalización del azúcar. Estos cambios se explican utilizando valores de temperatura de transición vítrea (T_g) de literatura de los sistemas relacionados (banana liofilizada, sacarosa y trehalosa amorfas) en varias HR. El uso de trehalosa en lugar de sacarosa en el baño osmótico, dio lugar a una importante ventaja tecnológica puesto que la cristalización de las muestras se llevó a cabo a una mayor HR que la banana liofilizada sin tratamiento osmótico o aquella osmóticamente tratada con sacarosa.

Abstract

Banana slices were osmotically dehydrated in 45% w/w sucrose or trehalose solutions and freeze-dried to a water activity (a_w) of about 0.10. Freeze-dried products were stored at different relative humidities (%RH) up to 100 days to detect moisture loss associated with sugar crystallization. Following an initial water uptake, loss of sorbed moisture content was observed depending on %RH and this was likely due to sugar crystallization. These changes were adequately explained using literature glass transition temperature (T_g) values of related systems (freeze-dried banana, amorphous sucrose and trehalose) at various RH. The use of trehalose instead of sucrose in the osmotic bath, resulted in an important technological advantage since crystallization of the freeze-dried samples took place at higher RH than either for plain banana or that osmotically treated with sucrose.

Palabras clave: Liofilización, sacarosa, trehalosa, osmosis, cristalización, temperatura de transición vítrea.

Keywords: Freeze-drying; sucrose; trehalose; osmosis; crystallization; glass transition temperature

1. Introduction

Osmotic dehydration is a process which reduces the water activity (a_w) of foods (mainly fruits) by placing them in contact with a concentrated solution of sugars. It is one of the most suitable methods to increase the shelf life of fruits and vegetables [1] and it is frequently used as a pre-treatment to improve the quality of fruits which will be afterwards dehydrated by air-drying or freeze-drying [2, 3].

Sucrose is used in osmotic dehydration of fruits because of its accessibility and sensory acceptability [4, 5]. But it has certain drawbacks which include non-enzymatic browning, since it can be easily hydrolyzed into reducing sugars (at acid pH) and its low glass transition temperature (T_g) which leads to sucrose crystallization even at low relative humidities (%RH). The use of trehalose instead of sucrose has been proposed to deal with these disadvantages [6].

Trehalose is a non-reducing sugar with a high chemical stability under low pH conditions, therefore, it does not react with amino acids or proteins by Maillard browning reaction [7-9]. T_g of trehalose is much higher than that of sucrose [10-12]; in the anhydrous state the T_g of trehalose is about 105–115ºC as compared to 60–62ºC for sucrose.

Knowledge of the kinetics of water sorption of dehydrated fruits is required to establish optimum conditions for packaging, storage and utilization [13]. However, freeze-dried fruits are non-equilibrium systems because at reduced moisture content they are supersaturated in sugars which may crystallize upon water sorption [10, 14].

It has been reported in the literature that sugars in amorphous food powders have a strong tendency to absorb surrounding water vapor. Once water is sorbed, the T_g of the powders decreases below the storage temperature and crystallization can occur, resulting in the release of sorbed water [14, 15]. The aim of present work was to carefully follow sorption behavior of dried banana products (Control, Sucrose added and Trehalose added) over a period as long as 100 days in order to detect any sugar crystallization which would be reflected in loss of moisture content.

2. Materials and Methods

Sample preparation and osmotic dehydration

Ripe bananas (*Musa sapientum,* from Ecuador) were peeled and cut into uniform slices (5mm thick, average diameter of 3cm) using a vegetable slicer. Slices were placed in a citric + ascorbic acid solution (0.5%, 0.25% w/v, respectively) for two minutes to retard enzymatic browning. Two different osmotic dehydration (OD) solutions were used: 45% (w/w) sucrose (Ledesma., Argentina) and 45% (w/w) trehalose (Ingredion, Argentina). Concentration used corresponded to the solubility limit of trehalose [16]. A fruit:solution ratio of 1:3 was used without agitation and samples were kept in 1L containers at room temperature (20 ± 2)ºC during six hours [17]. Then, banana slices were taken out from the osmotic medium, gently dried (with paper towels) to remove the excess of solution, placed on a drying tray (30 slices per tray for freeze-drying batch) and freeze-dried. Total soluble solids (ºBx) were measured before and after the OD procedure.

Freeze drying

A tray of banana samples (30 slices) was placed for 24h in a freezer at -20ºC. It was afterwards freeze-dried in a FIC Ll-I-E300-CRT freeze-dryer (FIC, Rificor, Argentina) operated with a freezing plate at -35°C. Once a vacuum below 200 μmHg was obtained (after 4 hours), the freezing plate was turned off and the drying process continued at room temperature (around 20 ºC) for a period of 40 hours.

Following freeze-drying three different kinds of samples were obtained: 1) Freeze-dried banana without osmotic treatment (named Control), 2) Freeze-dried banana with previous osmotic dehydration in sucrose (named Sucrose) and 3) Freeze-dried banana with previous osmotic dehydration in trehalose (named Trehalose).

Total soluble solids measurement (ºBx)

Total soluble solids (ºBx) content was determined in order to follow the evolution of the osmotic treatment. Samples were crushed into a paste before and after the osmotic treatment and °Bx were measured using hand refractometers (Model N-2 and Model N-3E, Atago, Japan). All measurements were made in triplicate and the average is reported.

Water activity

Water activity (a_w) was determined using an electronic dew point water activity meter Aqualab series 3 (Decagon Devices, Pullman, USA) operated as described in a previous work [16].

Measurement of water sorption

After freeze-drying, samples were milled and transferred into vacuum desiccators and

kept at (36±1)ºC over saturated salt solutions which provided constant relative humidity between 11% and 49% [18].

Water uptake by the different systems (Control, Trehalose and Sucrose) was determined periodically by changes in weight. Final equilibrium conditions were considered to be reached when the difference in weight of samples at intervals of three days was arbitrarily less than 0.0005 g [18]. Three replicate samples were used at each %RH and the average is reported.

Moisture content was determined by first drying the samples in desiccators over magnesium perchlorate at 36ºC followed by oven drying at 103ºC for 6 hours.

3. Results and Discussion

As shown in **Table 1**, after osmotic treatment in both sugars (trehalose or sucrose) banana samples had the same ºBx and final a_w; this was expected since both sugars have identical a_w lowering ability [16].

Table 1 – Variation of °Bx and a_w in banana slices before and after osmotic treatment for 6 hours in 45% (w/w) sucrose or trehalose solution at room temperature.

Sample*	°Bx (initial)	°Bx (final)	a_w (initial)	a_w (final)
Control	21 ± 1	-	0.970 ± 0.003	-
With Trehalose	21 ± 1	27 ± 2	0.976 ± 0.003	0.965 ± 0.003
With Sucrose	21 ± 2	28 ± 1	0.977 ± 0.003	0.966 ± 0.003

Moisture uptake and "equilibrium"

The course of moisture uptake with time at low RH % (11 % and 22 %) at 36ºC is shown in Figure 1a and 1b. The sorption behavior of all three systems was similar: after reaching a maximum, moisture content remained almost constant for up to 100 days, although very small changes with time were still observed. It is noteworthy that few researchers study the adsorption behavior of dried fruits for a long time as it was done in present work. Falade and Awoyele [19] studied the adsorption isotherms of fresh and oven-dried bananas (using the same gravimetric-static method) but followed kinetics only up to 14-17 days; after that time-period they considered equilibrium was reached. Tsami et al. [20] also used a relatively short time (15 days) for determining water sorption isotherms of different fruits.

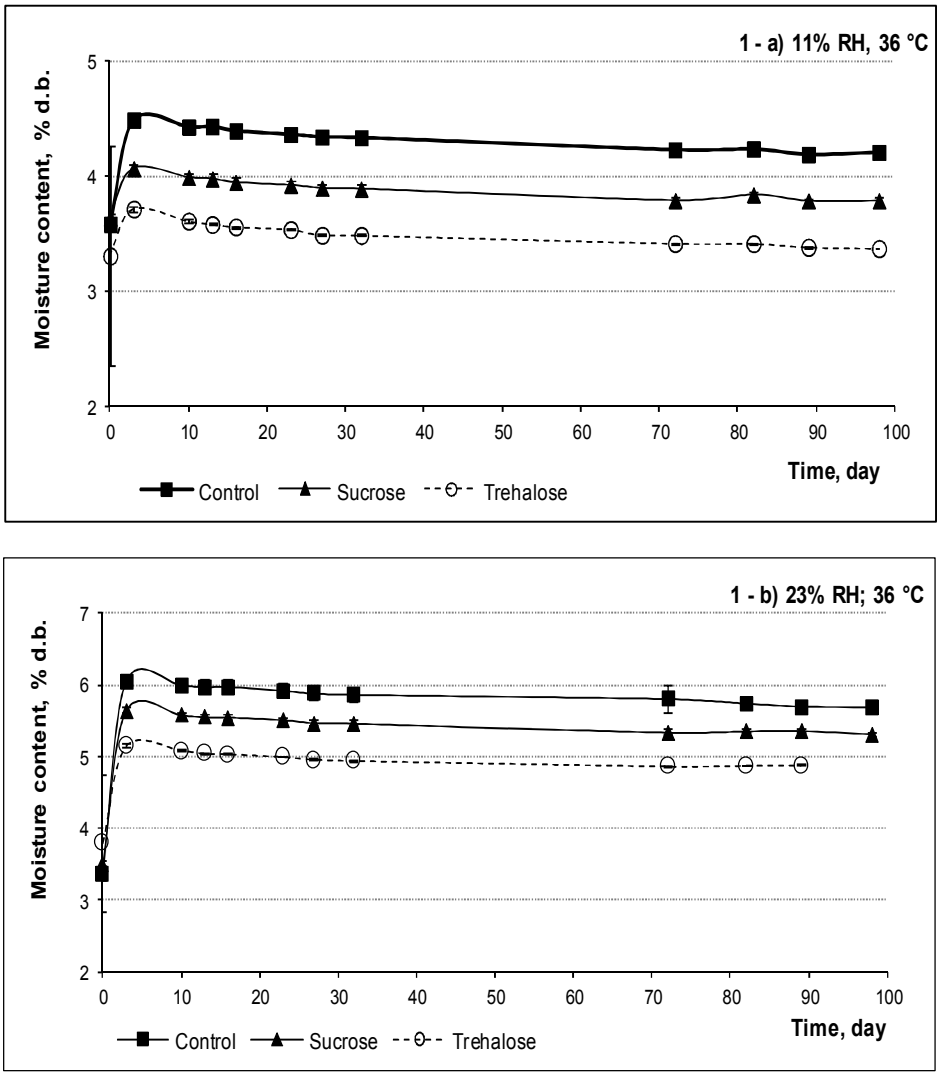

Figure 1a and 1b: Kinetics of water sorption at 36°C at 11 and 22% relative humidity of freeze-dried banana previously osmotically dehydrated with sucrose or trehalose. Standard deviation bars overlap with data points.

Moisture loss and sugar crystallization

At 33%RH (Figure 2 a) Control and Sucrose banana samples reached a maximum moisture content (around 9% dry basis) but then a progressive loss of moisture was observed from day 12 for Sucrose and from day 30 for Control. This was not observed in the Trehalose sample.

The behavior of freeze dried banana Control and Sucrose at 11, 22 and 33% RH had a striking similarity with the classical work of Makower and Dye [21] on crystallization of amorphous sucrose and glucose exposed to RH ranging from 4.6 to 33.6% at 25ºC. They found that at low relative humidities, moisture equilibrium was attained and practically no crystallization occurred in nearly 3 years. At higher humidities sugar crystallization with

subsequent release of moisture took place. More recently, Yu et al. [22] studied the moisture sorption behavior of freeze-dried amorphous sucrose using a dynamic humidity generating instrument (instead of a gravimetric static method). They also reported moisture-induced sucrose crystallization and that crystallization onset time decreased as %RH increased. Harnkarnsujarit and Charoenrein [15] studied sugar crystallization in freeze-dried mango powder stored at various RH and also reported sugar crystallization revealed by the loss of sorbed water in the water sorption experiment. X-ray powder diffraction and scanning electron microscopy were used to confirm the crystallization. Their results also showed that increased %RH resulted in higher sugar crystallization. The loss of adsorbed water due to sugar crystallization during storage at given %RH, had also been reported previously for other food powders, such as milk powders [23].

As also shown in Figure 1a and 1b, banana osmotically treated with trehalose did not experiment moisture loss in the time-period studied (100 days); this was likely due to the contribution of trehalose to the increase of glass transition temperature (T_g) of the system, as compared to sucrose.

Figure 2a also shows that the rate of moisture loss was higher in banana osmotically dried with Sucrose than in banana Control, which may be attributed to the different relative sugar composition of these systems. In ripe banana, glucose and fructose constitute about 80% of sugars and the rest is sucrose. In sample Sucrose, relative amount of sucrose is likely to increase due to sugar gain from the osmotic bath while glucose and fructose may be leached out. Figure 2b shows that all samples evidenced moisture loss when exposed to 43%RH. However, Iglesias et al. [18] showed that amorphous trehalose absorbs water with increasing RH, but the absorbed moisture levels out at 43%RH (i.e. the isotherm presents a plateau). The moisture content at this plateau is close to the amount of water needed to form the dihidrate (10.5% on dry tehalose basis) suggesting crystallization of trehalose. Consequently, the observed moisture loss at 43%RH must be attributed to the crystallization of other sugars present in banana, a phenomenon which is facilitated by trehalose crystallization which no longer contributes to increasing the T_g of the system. Figure 2c shows that at a slightly higher RH (49%) there was a similar behavior.

As previously mentioned, weight changes were monitored up to 100 days and a weight difference of 0.0005g between two consecutive measurements was arbitrarily set as equilibrium condition. However, although this condition was approached, it was not entirely reached in many cases (*quasi-equilibrium* condition); this was likely related to very slow sugar crystallization with associated moisture loss over time.

It is generally accepted that sugar crystallization is a time-dependent phenomenon which is a strong function of the difference between storage and glass transition temperatures (T_0-T_g), where T_0 is storage temperature [24]. However, in complex systems (like banana) crystallization does not depend only on T_0-T_g but also on interactions between the amorphous sugars and biopolymers present, as clearly demonstrated by several authors [14, 25]. Iglesias and Chirife [14] reported that in humidified freeze-dried model systems containing different biopolimers (alginate, starch, etc) crystallization of amorphous sucrose was strongly delayed in comparison to pure amorphous sucrose.

Analysis of results from T_g values from literature

Moraga et al. [26] reported a T_g value of 41.6ºC for freeze-dried banana at 11%RH. At the same %RH, Roos and Karel [27] and Iglesias et al [18] reported values of 37.4ºC and 65.0ºC for T_g of amorphous sucrose and trehalose respectively. All these T_g values are above storage temperature (36ºC), which explains the observed lack of crystallization in the systems showed in Figure 1 a.

T_g values found in the literature for dried banana at 23%RH range between 21 - 30ºC [26, 28]; and for pure amorphous sucrose at the same %RH, it is of 28ºC [27]. These values would tend to predict crystallization; however, since crystallization is a time-dependent phenomenon, T_0-T_g should be above 10ºC to observe crystallization in a reasonable time period [29]. For amorphous trehalose at 22% RH, Iglesias et al [18] reported a T_g value of 45ºC which would partially explain the lack of crystallization during storage at 36ºC (Figure 1 b).

At 33%RH, T_g of freeze-dried banana was reported around 8ºC [26] while for pure amorphous sucrose it was around 13ºC [27]; these values would explain the rapid crystallization for banana Control and Sucrose samples observed at this %RH (Figure 2a). At this same %RH pure amorphous trehalose has a T_g of 34ºC [18] which would explain the observed lack of crystallization. As mentioned before, at 43%RH (Figure 2b) T_g of trehalose decreases to 14ºC and its crystallization can take place, forming the dihydrate (Tr.2H_2O). After crystallization, trehalose is not able to inhibit the crystallization of other sugars present in banana.

The loss of sorbed water in the freeze-dried banana samples (Control, Sucrose and Trehalose) was attributed to crystallization of sugars other than trehalose. Sugars in these products are usually present in the amorphous state and have a strong tendency to absorb surrounding water vapor. Once water is sorbed, the T_g of the powders decrease below the storage temperature and crystallization can occur, resulting in the release of sorbed water. Trehalose does not release water upon crystallization since it forms a dihydrate. These changes were

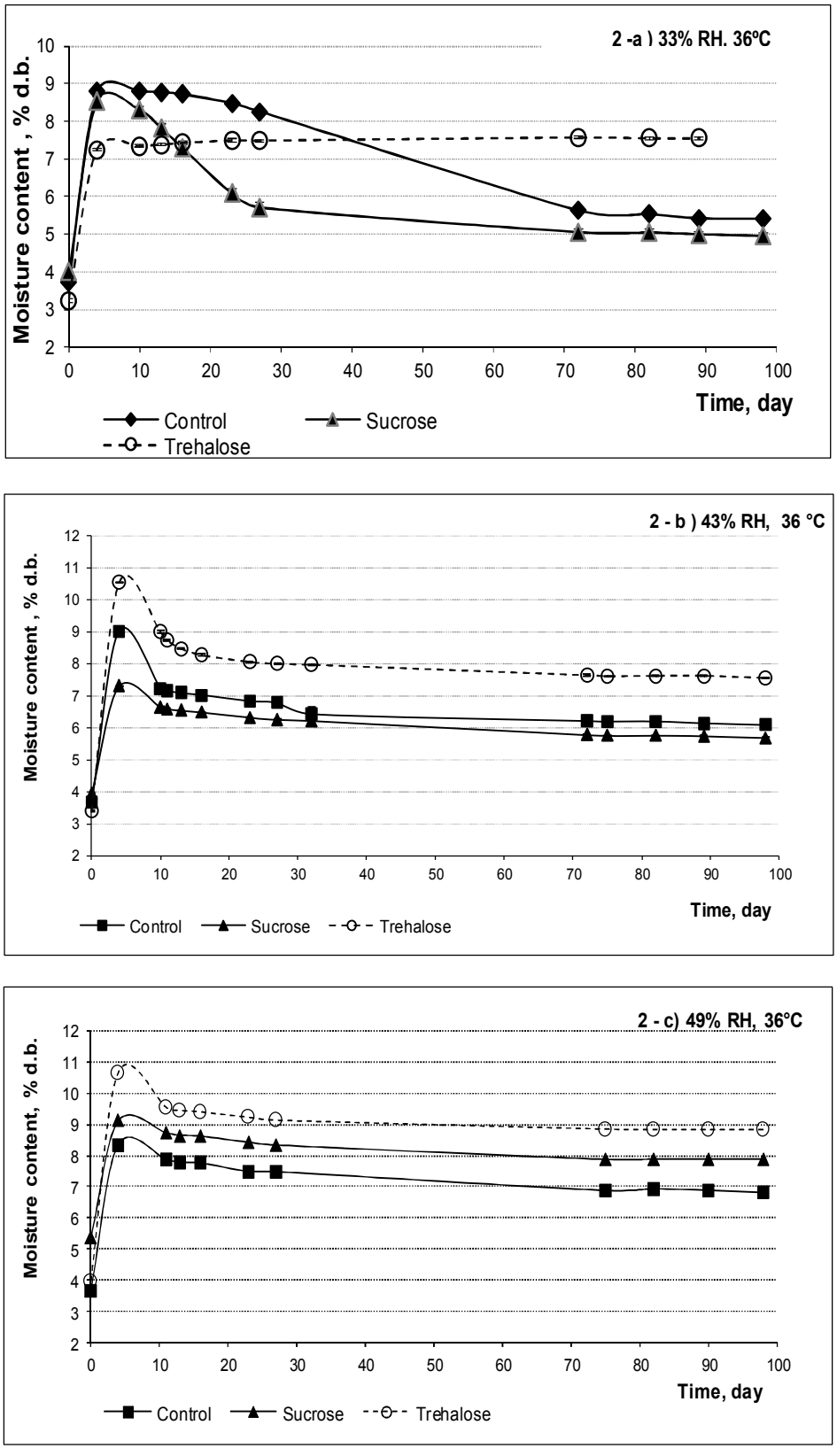

Figure 2a, 2b and 2c: Kinetics of water sorption at 36°C at 33, 43 and 49% relative humidity of freeze-dried banana previously osmotically dehydrated with sucrose or trehalose. Standard deviation bars overlap with data points.

adequately explained by literature T_g values of related systems (freeze-dried banana, amorphous sucrose and amorphous trehalose).

4. Conclusions

The use of trehalose instead of sucrose in the osmotic bath gave an important technological advantage; these freeze-dried samples crystallized at higher %RH than either simple banana or that osmosed in sucrose.

It was also observed that all water sorption data approached but did not entirely reach equilibrium values; in fact moisture content still changed (decreasing) very little with time, and this was attributed to slow crystallization. This stresses the importance of using long equilibrium times when determining adsorption equilibrium in dried fruits containing amorphous sugars likely to crystalize.

References

[1] A. K. Yadav, S. V. Singh, Journal of Food Science and Technology 51(2014) 1654-1673.
[2] A. Nieto, D. Salvatori, M. Castro, S. Alzamora, Journal of Food Engineering, 36 (1998) 63-79.
[3] C. Alvarez, R. Aguerre, R. Gomez, S. Vidales, S. Alzamora, L. Gerschenson, Journal of Food Engineering 25 (1995) 167-178.
[4] A. Nieto, D. Salvatori, M. Castro, S. Alzamora, Journal of Food Engineering 61 (2004) 269-278.
[5] A. Raoult-Wack, *Trends in Food Science & Technology* 5 (1994) 255-260.
[6] S. Vicente, A. Nieto, S. M. Alzamora, Effects of a w Reduction and Type of Sugar in Rheological Behavior, Water Mobility, and Structural Changes in Apples, in: G. F. Gutiérrez-López, L. Alamilla-Beltrán, M. del Pilar Buera, J. Welti-Chanes, E. Parada-Arias, and G. V. Barbosa-Cánovas (Eds), Water Stress in Biological, Chemical, Pharmaceutical and Food Systems, Springer, New York, 2015, pp. 375-382.
[7] C. Schebor, L. Burin, M. a. d. P. Buera, J. Chirife, LWT-Food Science and Technology 32 (1999) 481-485.
[8] D. Komes, T. Lovrić, K. Kovačević Ganić, J. Gajdoš Kljusurić, M. Banović, International Journal of Food Science & Technology 40 (2005) 425-435.
[9] D. Komes, T. Lovric, K. Kovacevic Ganic, L. Gracin, Food Technology. Biotechnology 41 (2003).
[10] Y. H. Roos, Food Technology 49 (1995).
[11] S. Rossi, M. P. Buera, S. Moreno, J. Chirife, Biotechnology progress 13 (1997) 609-616.
[12] A. Patist and H. Zoerb, Colloids and Surfaces B: Biointerfaces 40 (2005) 107-113.
[13] P. Udomkun, M. Nagle, D. Argyropoulos, B. Mahayothee, S. Latif, J. Müller, Food Chemistry 196 (2016) 712-719.
[14] J. Chirife and H. A. Iglesias, International Journal of Food Science & Technology 13 (1978) 159-174.
[15] N. Harnkarnsujarit and S. Charoenrein, Food Research International 44 (2011) 3188-3194.

[16] M. Galmarini, J. Chirife, M. Zamora, A. Pérez, LWT-Food Science and Technology 41 (2008) 628-631.
[17] C. D. M. Campos, A. C. K. Sato, R. V. Tonon, M. D. Hubinger, R. L. d. Cunha, Food Science and Technology (Campinas) 32 (2012) 357-365.
[18] H. A. Iglesias, J. Chirife, and M. P. Buera, Journal of the Science of Food and Agriculture 75 (1997) 183-186.
[19] K. Falade and O. Awoyele, Journal of Food, Agriculture and Environment 3 (2005) 97-102.
[20] E. Tsami, D. Marinos□Kouris, Z. Maroulis, Journal of Food Science 55 (1990) 1594-1597.
[21] B. Makower and W. Dye, Journal of Agricultural and Food Chemistry 4 (1956) 72-77.
[22] X. Yu, S. M. Kappes, L. A. Bello-Perez, S. J. Schmidt, Journal of Food Science 73 (2008) E25-E35.
[23] K. Jouppila and Y. H. Roos, Journal of Dairy Science 77 (1994) 2907-2915.
[24] Y. Roos and M. Karel, Food Technology 45 (1991) 66, 68-71, 107.
[25] P. Buera, C. Schebor, B. Elizalde, Journal of Food Engineering 67 (2005) 157-165.
[26] G. Moraga, P. Talens, M. Moraga, N. Martínez-Navarrete, Journal of Food Engineering 106 (2011) 212-219.
[27] Y. Roos and M. Karel, Biotechnology progress 6 (1990) 159-163.
[28] W. Sonthipermpoon, T. Suwonsichon, S. Wittaya-Areekul, P. Wuttijumnong, Natural Science 40 (2006) 708-15.
[29] B. Bhandari, T. Howes, Journal of Food Engineering 40 (1999) 71-79.

Journal of the Argentine Chemical Society

SUSTAINABLE BIODIESEL: KINETIC STUDY AND MODELING OF CATALYTIC ESTERIFICATION OF USED VEGETABLE OILS AS THE FIRST STAGE OF THE PRODUCTION PROCESS

Verónica Rodriguez[3], María F. Laborde[1,2,3], María C. Gely[2,3], Ana M. Pagano[2,3,*]

[1]*Consejo Nacional de Investigaciones Científicas y Técnicas (CONICET)*
[2]*Redes Interuniversitarias REDES VIII – Proy. 35-83-0096, Sec. de Pol. Universitarias (SPU), Min. de Educación de la Nación, Argentina*
[3]*Núcleo TECSE, Área de Procesos, Depto. Ing. Química, F. de Ingeniería, UNICEN, 7400 Olavarría, Argentina.*
** Corresonding. Author: apagano@fio.unicen.edu.ar/anamariapagano@gmail.com*

Received December 28th, 2016. Accepted in final form April 12th, 2017

Resumen

Con ánimo de contribuir a satisfacer las necesidades de producción sostenible de biocombustibles en procesos industriales, en el presente trabajo se ha estudiado la cinética de esterificación de aceites vegetales usados (UVOs) con etanol, empleando aceite de girasol acidificado. El proceso se llevó a cabo en un reactor discontinuo termostatizado con agitación magnética. Se ensayaron diferentes temperaturas (50, 60 y 70°C) y tiempos de reacción en el intervalo de 0-90 minutos. Se aplicó una relación molar de etanol / ácido oleico de 60: 1. El catalizador utilizado fue H_2SO_4 (5% p/p con respecto al contenido de ácidos grasos libres). Se determinó una conversión del 75,54% a 70°C. Estos datos cinéticos experimentales se utilizaron en la simulación del proceso completo de esterificación desarrollado en Aspen HYSYS® con resultados de conversión similares.

Abstract

In an attempt to satisfy the needs for sustainable production of biofuel in industrial processes, the present work develops the esterification kinetics of used vegetable oils (UVOs) with ethanol, employing acidified sunflower oil. The process was carried out in a thermostated batch reactor with magnetic stirring. Different temperatures (50ºC, 60ºC and 70°C) and reaction times in the range 0-90 minute were assayed. An ethanol/oleic acid molar ratio of 60:1 was applied. The catalyst used was H_2SO_4 (5% w / w relative to the free fatty acid). A conversion of 75.54% was determined at 70 °C. These experimental kinetic data were used in the simulation of the complete esterification process performed in Aspen HYSYS™ with similar conversion results.

Palabras Clave*: Biodiesel, esterificación catalítica, aceites vegetales usados, cinética de reacción.*

Keywords*: Biodiesel, catalytic esterification, used vegetable oils, reaction kinetics.*

1. Introduction

Without doubt, the demand for biofuels has recently increased in response to the current energy crisis and concern for the environment. Biodiesel is a type of biofuel that can be added to diesel of fossil origin, which is used mainly in transport, in different percentages. In Argentina, from 2010 onwards, the minimum proportion evolved from 5% to 10% [1-4].

Biodiesel is an alternative fuel that represents a source of contamination-free energy, as it is derived from renewable raw materials and produces low toxic emissions [5-7]. It can be obtained from the catalytic transesterification of used vegetable oils (UVOs), helping to solve two current problems: reuse of residues and the production of sustainable biofuels from non-conventional raw materials, reducing the use of edible oils.

UVOs embody an economical source of raw material for the production of biodiesel [8-10]. However, it should be considered that during frying, the oil is subjected to high temperatures of 180-190 °C [11], which has a negative effect on the properties of the oil with the formation of free fatty acids (FFA). A high level of FFA in the transesterification can cause the deactivation of the alkaline catalyst and a saponification reaction that hinders the separation of the reaction products [9].

In order to reduce the acidity of the raw material to a level lower than 0.5% free fatty acids (% FFA) a pretreatment must be employed [12]. The esterification method of free fatty acids with a short chain alcohol is one of the best treatments for the final production of esters [13]. Predominantly, methanol has been used in the production of biodiesel. This short chain alcohol is derived from fossil resources so the produced biodiesel can not be termed as fully renewable. Therefore, it is interesting to analyze the possibility of using ethanol for the production of biodiesel, since this alcohol can be obtained by fermentation from various energy crops rich in carbohydrates (such as potatoes, sugarcane, corn grains and sorghum) or other Renewable resources (such as food industry waste) [14]. The application of renewable raw materials and their efficient processing is crucial in the development of sustainable processes [15].

In the literature, there are numerous studies in which different processes of biodiesel production on an industrial scale have been simulated with the Aspen HYSYS™ software [16-19], using different raw materials and catalysts. No reports have been found in which the study of the esterification process of UVOs with ethanol through acid catalysis has been approached. Neumann et al. [15] performed an experimental analysis of the kinetics of the esterification reaction of used vegetable

oils for the production of biodiesel, using oleic acid (as descriptor of the UVOs) and using ethanol in a reactive distillation column.

The economic and environmental interest of the use of UVOs, the need for a fully sustainable biodiesel production and the importance of the characterization of the kinetics of the reaction with ethanol to optimize the sizing of the esterification reactor required in a process plant, are the aspects that lead the present study. The general objective is to examine the influence of operational variables (temperature, time) on the FFA esterification reaction of UVOs with ethanol by acid catalysis. The aim is to optimize the process and to develop an experimentally validated kinetic model to introduce in the simulation model of the reactor that forms part of the esterification process previously developed by Laborde et al. [20].

2. Materials and Methods

The esterification reaction was carried out using commercial sunflower oil as raw material. This oil was selected as representative of UVOs, based on statistical data of edible oils consumption in Argentina [21].

The experiments were performed with commercial sunflower oil acidified artificially by adding an organic acid, as was proposed by several researchers [12, 22, 23].

Taking into account that triolein is one of the main components present in the triglyceride composition of traditional sunflower oils and the principal fraction in high oleic sunflower oils, oleic acid was selected to be added to commercial sunflower oil with the purpose of increasing its acid value. This decision was also supported by the evidence that oleic acid is the main constituent of residual and non-edible cooking oils [24].

The use of the synthetic "used vegetable oil" properly prepared by this procedure prevented avoiding the potential interferences of other possible components of the oil with the reaction kinetics focused on here.

The acid value of the samples was approximately 6.5 mg KOH / g oil, slightly higher than the levels typically found in frying oils [12, 24].

The acidity value, expressed as mg KOH / g oil, was determined by following the technique of AOCS Ca 5a-40 [29], after washing the sample with distilled water to remove the residual catalyst.

The esterification of the FFA was performed with anhydrous ethanol using an ethanol:oleic acid ratio of 60:1. The catalyst used was sulfuric acid at a concentration of 5% by weight with respect to the total acidity (represented as oleic acid). These conditions of molar ratio of reactants and catalyst

concentration were defined on the basis of the optimum operating conditions determined by Berrios et al. [12] in its esterification study, using methanol in order to obtain an acidity level lower than 0.5% FFA (equivalent to 1 mg KOH / g oil).

The effect of temperature (T) was studied by carrying out the reaction at 50, 60 and 70 °C. These experiments were performed in a batch reactor of 500 mL equipped with magnetic stirring and temperature control. The stirring speed varied between 300 and 400 rpm (although this variable does not produce a significant effect on the reaction rate [1]). The volume of reaction mixture was 360 mL.

The kinetics of the reaction was evaluated along 120 minutes by extracting 40 mL samples at regular intervals. These intervals were pre-established by means of preliminary testing of the experimental technique (not shown in this paper). These intervals were set at 15 minutes for the first 30 minutes of reaction, and then extended to 30 minutes until the end of the process.

After the sample was taken, the reaction was dropped by the addition of an excess of water [23, 25]. This procedure was performed in order to synchronize the residual acidity measurement of the different samples taken at a given time and temperature.

The extracted samples were quantified by titration using the AOCS standard Ca 5a-40 [29]. All experiments were performed in triplicate.

The experimental results were analyzed statistically with the software SYSTAT™ V12, by analysis of the variance (ANOVA) to evaluate the influence of temperature and time of reaction, and by means of regression of least squares to model the curves of reaction.

From the adjustment of the experimental data a kinetic model was developed, which was incorporated to the design of the stationary-state esterification reactor that participates in the complete flow diagram process previously developed in the Aspen HYSYS™ environment [20].

3. Results and Discussion

The experimental data of acid value (45 points) were obtained for the different temperature conditions and reaction times tested. The free acidity curves as a function of time decreased for all temperatures. Figure 1 shows the temporal results of acidity values grouped by temperature as triplicate average, with their corresponding standard error bars.

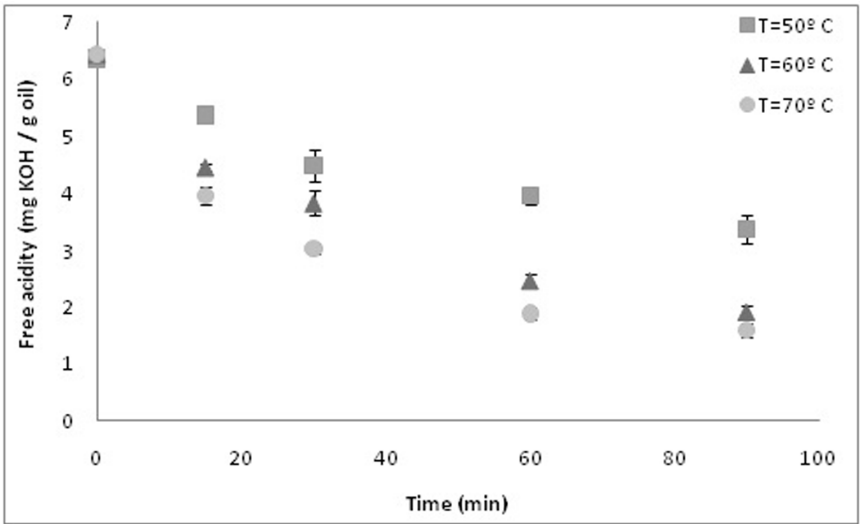

Fig.1. Variation of acidity value with temperature, using a sulfuric acid concentration of 5% w / w and an ethanol:oleic acid ratio of 60:1.

Effect of reaction temperature

The concentration of free fatty acids was measured throughout time. In the experimental trials, regardless the evaluated temporal range, it was observed that greater conversions of oleic acid were obtained at higher operating temperature, evidencing that the decrease in acidity was favored by the increase in temperature.

As an example, as shown in Fig. 1, at 30 min of reaction the acidity at 50 °C was 4.49 mg KOH / g oil while at 70 °C the acidity was 3.04 mg KOH / g oil, which demonstrates the above-mentioned statement.

The enthalpy of the esterification reaction at the reference temperature of 25 °C was theoretically calculated from the enthalpies of formation of the products and reagents. These enthalpies of formation were obtained from recognized databases (NIST, Chémeo, PubChem). As a result, a positive reaction heat value was obtained, which evidenced the endotherm of the reaction at 25 °C.

Subsequently, from this result and specific heat-temperature correlations obtained from the Aspen HYSYS™ library for each reaction component, the enthalpy of reaction at each temperature was evaluated, always proving to be positive with which it can be assumed that the reaction is endothermic in the range of the study.

Moreover, other available tools, which are described below, were used to analyze the heat of reaction.

The equilibrium conversions in the 50-70 °C range were obtained by means of two procedures: i) asymptotic extrapolation of the kinetic model that adjusts the experimental data that has been developed in this work for each temperature; and ii) by experimental determination of the equilibrium conversion for each temperature of the experimental design at long reaction times (>120 minutes). The data determined by these two procedures yielded congruent.

Using the resulting values, the reaction equilibrium constants for each temperature were calculated and the enthalpy of reaction in the study range was obtained by means of the van't Hoff equation, showing positive sign, which again offered support to verify the endothermicity of the reaction.

Simultaneously, a decreasing evolution of the temperature of the reaction medium was experimentally recorded by means of a laboratory calorimeter (Dewar vessel).

The statistical analysis of the variance performed on the set of experimental results showed that there was a significant effect ($\alpha = 0.05$) of the time ($p < 7.177\times10^{-12}$), reaction temperature ($p < 1.237\times10^{-11}$) and its interaction ($p < 1.073\times10^{-11}$) on the acidity value of the samples.

At 90-minutes reaction, different conversions of FAA, calculated as the ratio between remain moles and the initial moles of oleic acid [27, 23], were achieved at different working temperatures, as it can be seen in Table 1.

Table 1. Experimental conversions at 90 min of reaction

T (ºC)	Conversion (%)
50	46.81
60	70.09
70	75.27

Development of the kinetic model

Using the experimental data obtained at different temperatures, a kinetic analysis of the esterification reaction of fatty acids with ethanol was carried out. The reaction of a fatty acid with an alcohol is as follows:

$$R_1 - COOH + R_2 - OH \leftrightarrow R_1 - COO - R_2 + H_2O \qquad (1)$$

The reaction (1) expressed in generic form is:

$$A + B \leftrightarrow C + D \qquad (2)$$

The law of reaction velocity (2) [21] is presented in Equation (3):

$$\frac{-d[A]}{dt} = K_1.[A].[B] - K_2.[C].[D] \qquad (3)$$

where: K_1, K_2 are kinetic constants of the direct and reverse reactions, respectively; [A], [B], [C] and [D] are de molar concentration of the reactants and products; t is the reaction time.

In the experiments performed, the ethanol-oleic acid molar ratio was high enough to assume a constant concentration of ethanol throughout the process.

With this premise, it can be established that [B] is constant throughout the reaction, then:

$$K_1' = K_1.[B] = \text{constant} \qquad (4)$$

That is, the reaction becomes pseudo first order for the direct and second order reaction for the inverse reaction, as presented in Equation (5).

$$\frac{-d[A]}{dt} = K_1'.[A] - K_2.[C].[D] \qquad (5)$$

As shown in Carberry [21], considering that [C] and [D] are zero at the beginning of the reaction and that [A] = A0-E, where E is the amount of [A] that reacted (ie, acidity removed) and A0 the initial acidity, then equation (5) can be expressed as:

$$\frac{dE}{dt} = K_1'.(A_0 - E) - K_2.E^2 \qquad (6)$$

The integration of Equation (6) gives:

$$2.K_2.\alpha.t = \frac{\ln[A_0 + E.(\beta - 0.5)]}{[A_0 - E.(\beta + 0.5)]} \qquad (7)$$

where:

$$\alpha = \sqrt{\left(\frac{K_{eq}^{\,2}}{4}\right) + K_{eq}.A_0} \qquad (8)$$

$$\beta = \frac{\alpha}{K_{eq}} \quad \text{y} \quad K_{eq} = \frac{K_1}{K_2} \qquad (9)$$

Explaining E from the expression (7) gives:

$$E = \frac{2.A_0[e^{2.K_2.t.\alpha} - 1]}{e^{2.K_2.t.\alpha}.(2\beta + 1) + 2\beta - 1} \qquad (10)$$

The data experimentally obtained were adjusted by the statistical program SYSTAT™ V12 through Equations (7), (8) and (9). From this analysis, the kinetic constants were obtained for each experimental test (Table 2).

The influence of temperature on the constants of reaction rate can be determined by using Arrhenius's Equation (11):

$$K = A.\exp\left[\frac{-\Delta E}{R.Ta}\right] \qquad (11)$$

where: A is the pre-exponential constant; ΔE is the activation energy of the reaction; R is the constant of ideal gases (8.314 J/(mol-K)); Ta is the absolute temperature.

Table 2. Kinetic constants for direct and reverse reactions of each experiment

Trial	T (ºC)	K_1 (ASE*) (min^{-1})	K_2 (ASE*) (g oil / (min-mg KOH))
1	50	1.31×10^{-2} (2.14×10^{-3})	5.52×10^{-3} (1.25×10^{-3})
2	50	8.89×10^{-3} (8.60×10^{-4})	2.11×10^{-3} (8.00×10^{-4})
3	50	9.73×10^{-3} (4.90×10^{-4})	1.49×10^{-3} (3.70×10^{-4})
1	60	2.07×10^{-2} (6.00×10^{-4})	1.44×10^{-3} (1.00×10^{-4})
2	60	1.82×10^{-2} (1.44×10^{-3})	9.90×10^{-4} (2.90×10^{-4})
3	60	1.89×10^{-2} (1.27×10^{-3})	1.48×10^{-3} (2.60×10^{-4})
1	70	2.95×10^{-2} (1.12×10^{-3})	1.53×10^{-3} (1.00×10^{-4})
2	70	2.80×10^{-2} (4.40×10^{-4})	1.98×10^{-3} (5.00×10^{-5})
3	70	2.82×10^{-2} (1.23×10^{-3})	1.74×10^{-3} (1.20×10^{-4})

*ASE: standard error of the parameter (units of the parameter)

With the kinetic constants for each temperature and trial shown in Table 2, adjustment of Equation (11) was made with SYSTAT™ V12, from which it was possible to obtain the pre-exponential factor and the activation energy of the reaction, shown in Table 3.

Table 3. Activation energy and pre-exponential factor for direct and reverse reactions

Reaction	A (ASE*) (min^{-1})	ΔE (ASE*) (J/mol)
Direct	356817.60 (5.52)	46527.72 (4727.74)
Reverse	45.34 (157.18)	29008.51 (14213.50)

*ASE: standard error of the parameter (units of the parameter)

In Fig. 2 it is possible to observe that the reaction at 70 °C shows the best results in terms of decrease in acidity value in sunflower oil, due to the fact that it was performed at a higher temperature. However, these results reflect that it was not possible to obtain an acidity level lower than 1 mg KOH / g oil, which would be advisable to avoid the possible saponification reaction, the main disadvantage in biodiesel production.

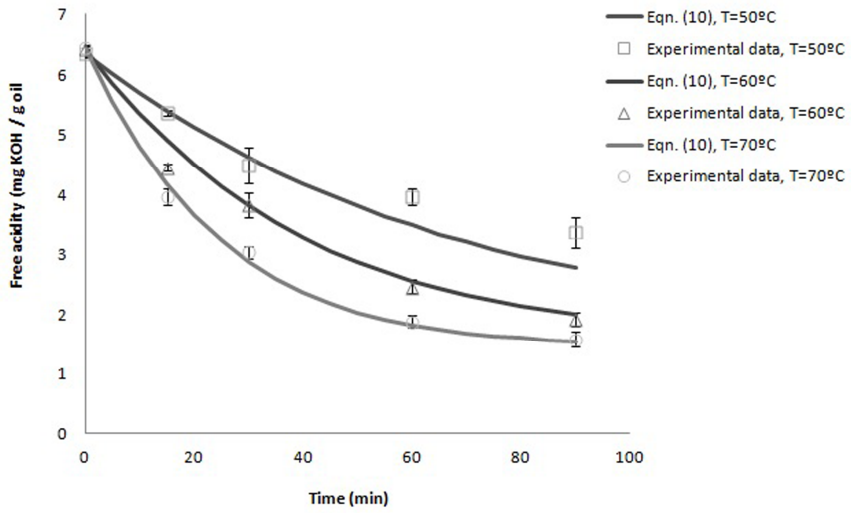

Fig. 2. Comparison between experimental data (points) and predicted curves of the kinetic model (lines).

In these experiments, the desired acidity of 1 mg KOH / g oil (equivalent to 0.5% FFA) resulted unattainable, obtaining an average final value in the experiment at 70 ºC of 1.59 mg KOH / g oil to the 90-min reaction. This datum becomes the starting point to postulate that, through the modification of some variables of the reaction, as such as the increase of the catalyst concentration, it would be possible to obtain better results in the reduction of acidity.

Another possibility to obtain greater conversion in the reaction to be considered for further research work involves the esterification in two stages, eliminating the water produced in the first stage, as its presence impair the reaction [27].

Modeling in Aspen HYSYS™

On the bases of the complete esterification process developed by Laborde et al. [20] the esterification step in Aspen HYSYS™ (Figure 3) was simulated with a kinetic reactor by substituting the previously applied conversion reactor. The new reactor was defined using the activation energy and pre-exponential factor obtained in this work, an ethanol: oleic acid molar ratio of 60:1, atmospheric pressure and a temperature of 70 °C.

From the design equation of an isothermal CSTR reactor (continuous stirred tank reactor) [28] a required volume of 6.26 m^3 was determined.

In the simulation of the process, a conversion was obtained in the kinetic reactor of 77.76% of the FFA at 70°C, only 2.7% higher than the experimentally obtained 75.54%.

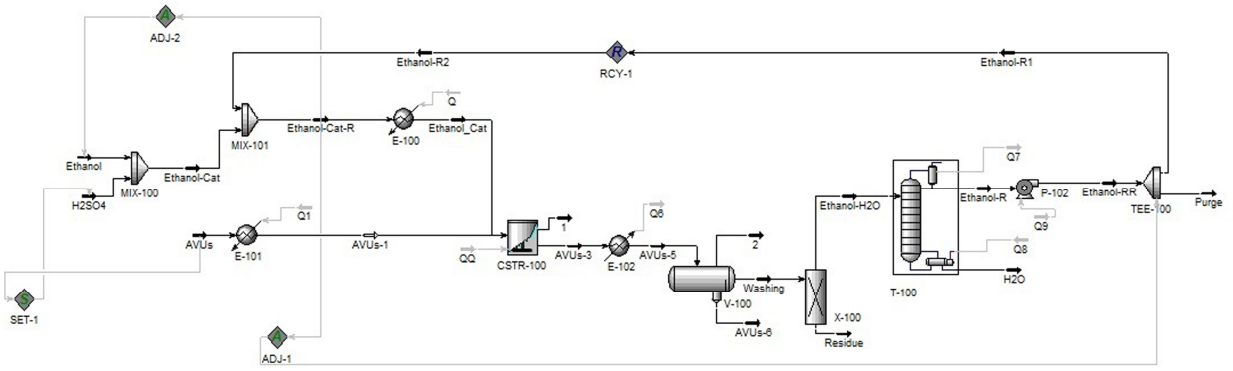

Fig. 3. Full esterification process of UVOs with ethanol

In order to compare the conversion of the reaction with ethanol and the results corresponding to methanol, the variation of the conversion of the FFA with the temperature was analyzed. For this purpose, Figure 4 was constructed by varying the temperature from ambient to the temperature near the boiling point of each alcohol (maximum working temperature at atmospheric pressure). The variation of the conversion as a function of T for esterification with ethanol was obtained by simulation, while the conversion of the reaction using methanol was calculated from the kinetics obtained by Berrios et al. [12].

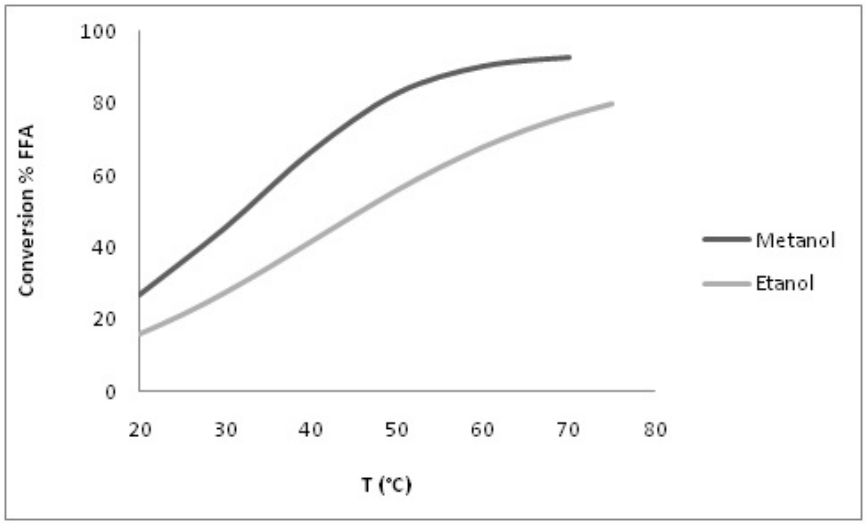

Fig. 4. Variation of FFA conversion as a function of reactor temperature for reaction with ethanol compared with that for methanol

It can be seen that the methanol conversion at the optimum process temperature (60 °C) is 13.46% greater than that obtained with ethanol at 70 °C (90.23%).

Despite the lower conversion of the reaction to ethanol under these working conditions, it is advisable to use ethanol instead of methanol. Ethanol is a renewable resource, and in addition, its handling is safer because it is less toxic than the latter. Besides, it improves the cold behavior properties of biodiesel, since the ethyl esters have a lower freezing point than the methyl esters.

4. Conclusions

The pre-exponential factor and the activation energy for the direct and reverse esterification reactions of UVOs with ethanol were determined from experimental data. The best working temperature for the esterification with ethanol catalyzed with 5% w / w H_2SO_4 was 70 °C, obtaining a conversion of 75.54%. This reflects that it was not possible to obtain an acidity below 1 mg KOH / g oil (0.5% FFA), which is normally recommended to avoid the saponification reaction during the subsequent transesterification. Thus, to achieve a decrease in the level of free fatty acids up to a recommended value, it is suggested for subsequent studies to implement increase in the concentration of catalyst or to perform the esterification in two stages, by eliminating the water produced in the first stage, as its presence impairs the reaction. The reaction with ethanol, despite its lower conversion in comparison with methanol, is recommended since, unlike methanol, ethanol is a renewable resource, its handling is safer as it is less toxic, and it improves the cold behavior properties of biodiesel, the ethyl esters having a lower freezing point than the methyl esters.

References

[1] Resolución Nº 660/2015: Acuerdo de Abastecimiento de Biodiesel para su Mezcla con Combustibles Fósiles en el Territorio Nacional. Ratificación., in Resolución 6602015, InfoLEG: República Argentina DOI: http://servicios.infoleg.gob.ar/infolegInternet /anexos/250000-254999/251066/norma.htm.

[2] Resolución Nº 1125/2013, in Resolución Nº 11252013, InfoLEG: República Argentina,DOI: http://servicios.infoleg.gob.ar/infolegInternet/anexos/220000-224999/ 224799/norma.htm.

[3] UNR, O.E.S. *Aceites & Grasas (A&G)* **2016**, *1*, 46.

[4] Babazadeh, R.; Razmi, J.; Pishvaee, M.S.; Rabbani, M. *Omega* **2017**, *66*, 258.

[5] Hwang, J.; Bae, C.; Gupta, T. *Fuel* **2016**, *176*, 20.

[6] Flores Velázquez, R.; Muñoz Ledo Carranza, R.; Villalb Valle, D. *Investigación. Ingeniería y Tecnología* **2010**, *10*, 35.

[7] Nasir, N.F.; Daud, W.R.W.; Kamarudin, S.K.; Yaakob, Z. *Renewable and Sustainable Energy Reviews* **2013**, *22*, 631.

[8] Banerjee, A.; Chakraborty, R. *Resources, Conservation and Recycling* **2009**, *53*, 490.

[9] Wang, L.; Dong, X.; Jiang, H.; Li, G.; Zhang, M. *Bioresource Technology* **2014**, *158*, 392.

[10] Yaakob, Z.; Mohammad, M.; Alherbawi, M.; Alam, Z.; Sopian, K. *Renewable and Sustainable Energy Reviews* **2013**, *18*, 184.

[11] Hamilton, R.J.; Perkins, E.G. *A&G Magazine* **2002**, *3*, 292.

[12] Berrios, M.; Siles, J.; Martín, M.A.; Martín, A. *Fuel* **2007**, *86*, 2383.

[13] Boffito, D.C.; Pirola, C.; Galli, F.; Di Michele, A.; Bianchi, C.L. *Fuel* **2013**, *108*, 612.

[14] Verma, P.; Sharma, M.P. *Fuel* **2016**, *180*, 164.

[15] Neumann, K.; Werth, K.; Martín, A.; Górak, A. *Chemical Engineering Research and Design* **2016**, *107*, 52.

[16] Zhang, Y.; Dubé, M.A.; Mclean, D.D.; Kates, M. *Bioresource Technology* **2003**, *89*, 1.

[17] Zapata, C.D.; Martínez, I.D.; Castiblanco, E.A.; Henao Uribe, C.A. *Dyna* **2007**, *151*, 71.

[18] Made in Argentina. 24/04/2014; DOI: http://www.made-in-argentina.com/empresas/898/alimentos-y-bebidas-aceites-aceite-de-maiz.

[19] West, A.H.; Posarac, D.; Ellis, N. *Bioresource Technology* **2008**, *99*, 6587.

[20] Laborde, M.F.; Serna Gonzalez, M.; Pagano, A.M.; Gely, M.C. CLICAP **2015** (Congreso Latinoamericano de Ingeniría y Ciencias Aplicadas), **2015**. San Rafael, Mendoza, Argentina

[21] CIARA, Cámara de la Industria Aceitera de la República Argentina, **2017**.

[22] Cardoso, A.L.; Gonzaga Neves S.C.; da Silva, M.J. *Energies* **2008**, *1*, 79.

[23] Marchetti, M.; Pedernera M.N.; Schbib, N.S. *International Journal of Low-Carbon Technologies* **2011**, *6*, 38.

[24] Neumann, K.; Werth, K.; Martín, A.; Górak, A. *Chemical Engineering Research and Design* **2016**, *107*, 52.

[25] Ávila Gómez, A.E. Desarrollo de la cinética química de la reacción de transesterificación de la oleína de palma, Tesis Magister en Ingenieria Mecánica, Universidad del Norte, Barranquilla, Colombia, **2006**.

[26] Carberry, J. Chemical and Catalytic Reaction Engineering, Mcgraw-Hill, Inc., **1976**.

[27] Canakci, M.; Van Gerpen, J. *Trans. ASAE* **2001**, *44,* 1429.

[28] Levenspiel, O., Ingeniería de las Reacciones Químicas, Editorial Reverté, S.A, **1998**.

[29] AOCS Ca 5a-40, AOCS. Official Methods and Recommended Practices of the American Oil Chemists' Society, 4th edn., D. Firestone (Eds.), American Oil Chemists' Society, Champaign, **1989**.

Journal of the Argentine Chemical Society

DENSITY FUNCTIONAL THEORY (DFT) STUDY OF H_2S INTERACTIONS ON THE Pr-DOPED CeO_2(111) SURFACE

Alejandro Kinbaum[1], Eduardo Poggio-Fraccari[1,2], Fernando Mariño[1,2], Beatriz Irigoyen[1,2*]

[1] *UBA. Dto. de Ingeniería Química, Ciudad Universitaria, (1428) Buenos Aires, Argentina.*

[2] *CONICET- UBA, I. de Tec. del Hidrógeno y Energías Sostenibles (ITHES). Buenos Aires, Argentina.*

** Corresponding author. E-mail: beatriz@di.fcen.uba.ar*

Received February 27th, 2017. Approved April 18th, 2017.

Abstract

In this work, we performed a density functional theory (DFT) study of the H_2S interactions on a low praseodymium (Pr)-doped CeO_2(111) surface. For this study, we considered a 3.7 at% Pr doping and conducted DFT calculations using the GGA formalism with the 'U' correction on Ce(4f) and Pr(4f) orbitals. The H_2S molecule weakly interacts on both the stoichiometric and oxygen deficient (111) surface of undoped CeO_2 (ceria). However, on the $Ce_{0.963}Pr_{0.037}O_2$(111) surface with an oxygen vacancy (O-hole site near to Pr dopant), the presence of praseodymium promotes the dehydrogenation process with formation of HS and H species.

Resumen

En este trabajo presentamos un estudio basado en la teoría del funcional de la densidad (density functional theory, DFT) de las interacciones del H_2S sobre la superficie CeO_2(111) dopada con un bajo contenido de praseodimio (Pr). Para este estudio, se consideró un dopado de 3,7 at% de Pr y se efectuaron cálculos DFT usando el formalismo GGA e introduciendo la corrección 'U' sobre los orbitales Ce(4f) y Pr(4f). La molécula H_2S interactúa débilmente en la superficie CeO_2(111) sin dopar, tanto estequiométrica como deficiente de oxígeno. Sin embargo, en la superficie $Ce_{0.963}Pr_{0.037}O_2$(111) con una vacancia de oxígeno (sitio O-hole cerca del dopante Pr), la presencia de praseodimio promueve el proceso de deshidrogenación con la formación de las especies HS y H.

Palabras Clave: *Sulfuro de hidrógeno; Óxido de cerio; Praseodimio; Cálculos DFT+U*

Keywords: *Hydrogen sulfur; Cerium oxide; Praseodymium; DFT+U calculations*

1. Introduction

In the last decades, the search for new energy sources and alternative fuels are mainly forced by increasing concerns related to greenhouse gas emissions, finite availability of fossil combustibles, as well as health and safety considerations [1–3]. Hydrogen (H_2) is considered an environmentally friendly fuel and it can be produced from renewable resources such as biomass with low pollution and high efficiency.

Algae biomass has several advantages compared to other renewable energy sources: increased growing speed, high yield per surface unit [4], very efficient capture of carbon dioxide [5] and solar energy conversion [6], no-competence with the biomass used for food, and the possibility of growing in open waters [7]. Moreover, microalgae can employ the nutrients present in liquid urban residues to grow and, at the same time, pre-treating them [8].

Gasification of the algae biomass releases a stream containing CH_4, H_2, CO, CO_2, hydrocarbons of low molecular weight as well as several compounds with sulfur and nitrogen. This stream can be transformed into syngas (CO and H_2) and even improve its H_2 content through catalytic processes. However, these transformations involve not only CH_4 reforming but also prevention of catalysts deactivation by poisoning with sulfur-containing species.

Sulfur has a high negative impact on the several catalysts employed in industrial processes [9,10]. This negative effect can be mitigated removing most of the sulfur-containing species with hydro desulfurization catalysts or oxide adsorbents [11], but the associated energetic cost is very high. On the other hand, development of new catalysts with high sulfur tolerance represents an easier and less expensive alternative [12].

Sulfur is a poison for the metals of group VIII and especially causes severe deactivation of nickel [13]. Indeed, all the sulfur presents as H_2S can easily chemisorb on available Ni sites under CH_4 reforming reaction conditions.

As regard of Ni supports, Al_2O_3 is one of the most employed for Ni-based catalysts [14]. Particularly, better performance and sulfur tolerance has been reported for those Ni and noble metal catalysts supported on CeO_2 and CeO_2-ZrO_2 mixed oxides [15]. These features are mainly attributed to the good oxygen donation ability of CeO_2, originated by an easy transition of Ce cations oxidation state from Ce^{4+} to Ce^{3+} [16].

Therefore, the stability and catalytic performance of Ni active phase can be substantially improved by using a support based on CeO_2 [17]. In this regard, it is worth to note that the addition of praseo-

dymium into ceria lattice remarkably improves the oxygen storage capacity (OSC) of CeO_2 [18]. Thus, Pr-doped CeO_2 materials would promote the oxidation of H_2S, the most common sulfur-containing species and, so, be useful supports for the Ni active phase by preventing its deactivation due to sulfur poisoning.

By the way, as far as we know there are no previous theoretical studies of H_2S interactions on Pr-doped CeO_2 solid solutions. Therefore, in this work we performed density functional theory (DFT) calculations to evaluate H_2S interactions on a low Pr-doped CeO_2(111) surface.

2. Theoretical Methods

Cerium oxide (CeO_2, *ceria*) crystallizes in fluorite structure consisting of a face-centered cubic (fcc) system of Ce^{4+} cations with O^{2-} anions filling its tetrahedral holes. Experimental data indicated a lattice parameter value of 5.41 Å for this structure [19].

Concerning our work, optimization of the ceria bulk structure within a plane wave basis cutoff energy of 480 eV, led to a calculated lattice constant value of 5.50 Å. Then, the ideal model of the CeO_2 surface was constructed by cleaving the optimized bulk cell with the (111) plane and retaining an extra oxygen layer. We choose the (111) surface because it is the most stable among the low-index (111), (110) and (100) ones, and corresponds to minimal Ce–O bonds cleavage [20–22]. After that, the low-doped Pr-ceria surface was obtained from a CeO_2(111) slab, with a p(3x3) expansion of the surface unit cell, by substituting one surface Ce cation by Pr. This substitution allowed us to build the 3.7 at% Pr-doped CeO_2(111) surface.

Figure 1, shows the resulting $Ce_{0.963}Pr_{0.037}O_2$(111) surface. So, we can see the upper three atomic layers, an O-Ce-O sandwich formed by top O anions, surface Ce cations and subsurface O anions.

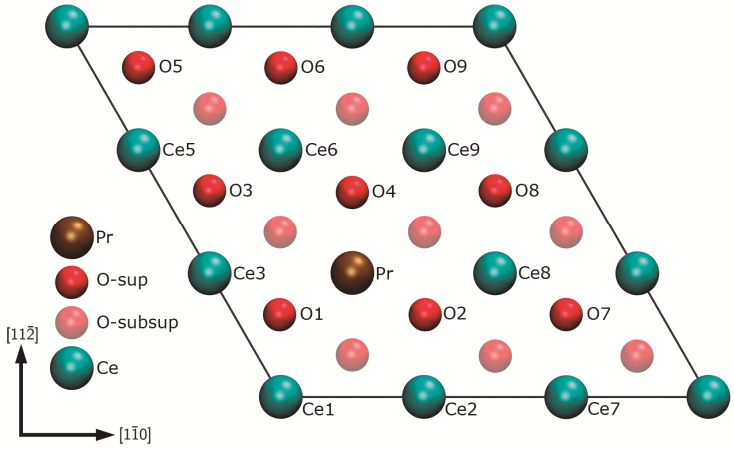

Figure 1. Front view of the stoichiometric $Ce_{0.963}Pr_{0.037}O_2$(111) surface.

The density functional theory (DFT) calculations were performed with the Vienna Ab-initio Simulation Package (VASP) [23,24]. The Kohn-Sham equations were solved with the generalized gradient approximation (GGA), and the exchange correlation functional of Perdew-Burke-Ernzerhof (PBE). Geometries were optimized until the Hellmann-Feynman forces converged to less than 0.02 eV/Å. The cutoff energy of the plane wave basis was set to 480 eV, and the core electrons were represented with the projector augmented wave (PAW) method using Ce($5s^2$, $5p^6$, $6s^2$, $5d^1$, $4f^1$), Pr($5s^2$, $5p^6$, $6s^2$, $5d^1$, $4f^2$) and O($2s^2$, $2p^4$) configurations for valence electrons. Self-consistent calculations were performed sampling the Brillouin zone with a 3×3×1 k-points grids under the Monkhorst-Pack scheme [25]. The different configurations were optimized using spin polarization calculations.

The standard DFT formulation usually fails to describe strongly correlated electrons in Ce(4f) and Pr(4f) orbitals, due to a deficient treatment of electron correlations. This limitation can be corrected to some extent by using the DFT + U method, where the introduction of a Hubbard parameter 'U' modifies the electron self-interaction error and enhances the description of the correlation effects. Accordingly, we used the Hubbard parameters: U_{eff} = 5 eV for Ce(4f) states, and U_{eff} = 4.5 eV for Pr(4f) orbitals. The value U_{eff} = 5 eV was chosen for the Ce(4f) states as it correctly described the atomic and electronic structure of both CeO_2 and CeO_{2-x} systems [26–28]. On the other hand, the value U_{eff} = 4.5 eV was considered reliable for describing the strong onsite Coulomb repulsion among Pr(3d) electrons, as it has shown to reproduce the experimentally available data for PrO_2 such as lattice constant and band gap [29].

Moreover, oxidation states and spin polarization were computed for different ions of interest by performing Bader charge and spin charge density analysis [30–32].

3. Results and Discussion

We began our study calculating the H_2S interactions on the stoichiometric $Ce_{0.963}Pr_{0.037}O_2$(111) surface. For this, we considered different active sites: surface O anions as well as Ce^{4+} and Pr^{4+} cations. As it can be seen in Fig. 1, surface O1, O3 and O6 sites have different cationic environment. The oxygen O1 is located inside a triangle formed by Ce and Pr cations (Ce1, Ce3 and Pr). The O3 anion is located near Pr, but surrounded by Ce cations (Ce3, Ce4 and Ce5). Meanwhile, O6 is also in the center of a triangle formed by Ce cations (Ce2, Ce5 and Ce6) but located far away from Pr.

Then, we evaluated H_2S interactions on the oxygen deficient $Ce_{0.963}Pr_{0.037}O_{2-x}$(111) surface, with O1 vacancy, by considering Pr (Pr^{3+}), Ce4 (Ce^{4+}) and Ce3 (Ce^{3+}) sites.

The H_2S adsorption energy (ΔE_{ads}) on the stoichiometric $Ce_{0.963}Pr_{0.037}O_2$(111) was computed as:

$$\Delta E_{ads} = E[H_2S/Ce_{0.963}Pr_{0.037}O_2(111)] - E[Ce_{0.963}Pr_{0.037}O_2(111)] - E[H_2S].$$

In this equation, $E[H_2S/Ce_{0.963}Pr_{0.037}O_2(111)]$ represents the total energy of the system formed after H_2S molecular interactions on the stoichiometric surface, $E[Ce_{0.963}Pr_{0.037}O_2(111)]$ is the total energy of the stoichiometric surface, and $E[H_2S]$ is that of the H_2S molecule in vacuum.

On the other hand, H_2S adsorption energy on the oxygen deficient $Ce_{0.963}Pr_{0.037}O_{2-x}(111)$ surface, with O1 vacancy, was calculated as:

$$\Delta E_{ads} = E[H_2S/Ce_{0.963}Pr_{0.037}O_{2-x}(111)] - E[Ce_{0.963}Pr_{0.037}O_{2-x}(111)] - E[H_2S].$$

In this equation, $E[H_2S/Ce_{0.963}Pr_{0.037}O_{2-x}(111)]$ represents the total energy of the system formed after H_2S interaction on the O-deficient surface, $E[Ce_{0.963}Pr_{0.037}O_{2-x}(111)]$ is the total energy of the O-deficient surface, and $E[H_2S]$ is that of the H_2S molecule in vacuum.

3.1 H_2S interactions on the stoichiometric $Ce_{0.963}Pr_{0.037}O_2(111)$ surface

Molecular H_2S interactions on the stoichiometric $Ce_{0.963}Pr_{0.037}O_2(111)$ are very weak. The interaction of H_2S on surface oxygen anions is a physisorption as indicated by the low adsorption energy value $\Delta E_{ads} = -0.14$ eV, and the long O–S distance which was calculated in 3.51 Å. The molecular interactions of H_2S on Ce2 (a Ce^{4+} cation near to Pr) or Ce4 (a Ce^{4+} cation close to Pr) are very similar as we calculated similar adsorption values for both physisorptions: $\Delta E_{ads} = -0.34$ eV, and Ce3–S and Ce4–S distances of 3.20 Å and 3.22 Å, respectively. For the Pr site, we calculated an H_2S adsorption energy $\Delta E_{ads} = -0.31$ eV and a Pr–S distance of 3.23 Å.

For comparison, we also computed H_2S interactions on the undoped $CeO_2(111)$ surface. The molecular interaction on a Ce site is also a physisorption ($\Delta E_{ads} = -0.21$ eV and d(Ce–S) = 3.20 Å). Meanwhile, we computed no interactions of the H_2S molecule on O sites ($\Delta E_{ads} = -0.01$ eV. Thus, we underline that our results indicating very weak interactions of H_2S molecule on Ce cations ($\Delta E_{ads} = -0.21$ eV) are in good agreement with previous reported energies values for adsorbed H_2S species on the $CeO_2(111)$ surface of about –0.1 eV [33].

Concerning the electronic structure of the stoichiometric $Ce_{0.963}Pr_{0.037}O_2(111)$ surface, Bader charge calculations for Ce and Pr cations gave values of 9.6e and 10.69e, respectively, and the computation of spin magnetization resulted in 0 B for Ce cations and 1.2 B for Pr one [18].

For the different optimized $H_2S/Ce_{0.963}Pr_{0.037}O_2(111)$ systems, our Bader charge and spin magnetization calculations show no changes of the surface electronic configuration which confirm the physisorptive character of molecular H_2S interactions on the stoichiometric $Ce_{0.963}Pr_{0.037}O_2(111)$ surface.

Thus, it is possible to assume that the H_2S molecule is weakly bound to both the undoped and Pr-doped stoichiometric $CeO_2(111)$ surface. The small calculated binding energy corresponds to a physisorption, and this H_2S weakly bond molecule could be considered as an intermediate to more stable species.

3.2 H_2S interactions on the $Ce_{0.963}Pr_{0.037}O_{2-x}(111)$ surface with a vacancy of O1

Praseodymium doping significantly reduces the energy required for anionic defects formation on the ceria surface. The calculated energy value for creation of the O1-defect on the $Ce_{0.963}Pr_{0.037}O_2(111)$ surface is about 1 eV [18], in agreement with that reported for the $Ce_{0.9688}Pr_{0.0312}O_{1.9688}$ bulk structure [34]. This finding agrees with the increase of oxygen vacancies concentration reported for Pr-doped CeO_2 solids [35–37].

The creation of the O1 vacancy on the $Ce_{0.963}Pr_{0.037}O_2(111)$ surface reflected in atomic relaxations of surface and subsurface ions. The distance from Ce1 cation to O1-hole was elongated ~ 10% compared to the Ce1–O1 bond length in the stoichiometric Pr-substituted $CeO_2(111)$ surface [18]. Similarly, Ce3 and Pr distances to O1-hole resulted 7% larger than those to O1. Cerium cations like Ce1, Ce3 and Pr also relaxed moving 0.25 Å, 0.19 Å and 0.20 Å, respectively, away from the O1-hole.

The electronic structure of $Ce_{0.963}Pr_{0.037}O_{2-x}(111)$ surface with the O1 vacancy was characterized trough Bader charge and spin polarization analyses. Bader charge calculations show 9.92e for the Ce3 cation and 10.96e for Pr one, indicating that the two electrons left in the solid after formation of O1-defect were transferred to the closest Ce cation (Ce3) and the Pr dopant [18]. Accordingly, spin magnetization values of Ce3(4f) and Pr(4f) orbitals were calculated in about 1 B and 2 B, respectively.

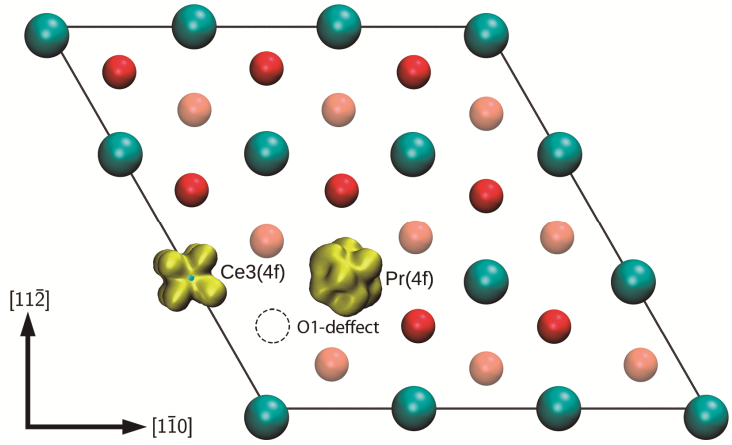

Figure 2: Electronic structure of the $Ce_{0.963}Pr_{0.037}O_{2-x}(111)$ surface with O1-defect. Spin polarization at a 0.05 e $Å^{-3}$ isovalue for Ce3(4f) and Pr(4f) orbitals. Positive and negative values are indicated in yellow and gray, respectively.

As regard of this electronic structure, Fig. 2 shows the isosurface of spin-polarized density for Ce3(4f) and Pr(4f) orbitals at a 0.05 e $Å^{-3}$ isovalue. As it can be seen, this isosurface also indicates that creation of O1-defect led to reduction of Pr and Ce3 cations.

Our study of H_2S interactions on the reduced $Ce_{0.963}Pr_{0.037}O_{2-x}(111)$ surface with an oxygen vacancy indicates that the H_2S molecule chemisorbed on the reduced cations. On the O-defective surface with a O1-hole, we computed strong adsorption energy values due to molecular H_2S interactions on Ce3 and Pr cations: $\Delta E_{ads} = -1.98$ eV on Pr^{3+} cation and $\Delta E_{ads} = -1.96$ eV on Ce3 (a Ce^{3+} cation). Together with these energy values, the distance between sulfur and Pr or Ce3 cations were calculated as follow: d(S–Pr) = 3.14 Å and d(S–Ce3) = 3.02 Å.

As well, we noticed that one of the H-S bonds was broken due to H_2S interaction on the O1-hole. Indeed, the first dehydrogenation of H_2S began with the molecule tilting towards the surface followed by the cleavage of one of the H–S bonds. Then, the process continues with the binding of this H fragment to the nearest oxygen anion and the sideways slipping of the HS species over the O1-hole.

Figure 3 displays the optimized atomic configuration for the HS-H/$Ce_{0.963}Pr_{0.037}O_{2-x}(111)$ system. Note that the HS fragment (d(H–S) = 1.35 Å) is over the O1-hole, while the H one is bound to lattice O^{2-} anion forming a hydroxyl species (d(H–O) =0.97 Å).

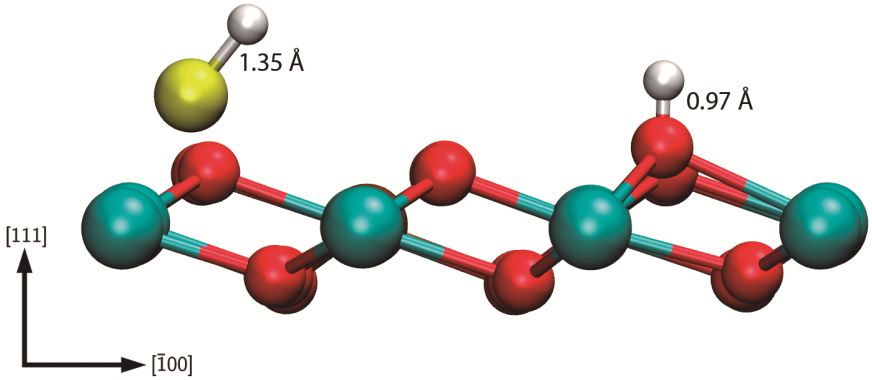

Figure 3: HS and H fragments adsorbed on the $Ce_{0,963}Pr_{0,037}O_{2-x}(111)$ surface with O1-defect

On the other hand, Bader charge calculations for the HS-H/$Ce_{0.963}Pr_{0.037}O_{2-x}(111)$ system indicate that only Ce3 (9.92e) and Pr (10.96e) are in the (3+) oxidation states. Accordingly, Ce and Pr cations show spin magnetizations of 1 B and 2 B, respectively. Thus, after adsorption of the HS and H fragments on the O-defective surface no new reduced cations were detected. This electronic struc-

ture is consistent with the isosurface of spin-polarized density shown in Fig. 4 for Ce3(4f) and Pr(4f) orbitals.

Altogether, our findings reveal a heterolytic cleavage of the H–SH bond into H^+ and HS^- species due to interaction of the H_2S molecule on the O-defective $Ce_{0.963}Pr_{0.037}O_{2-x}$(111) surface.

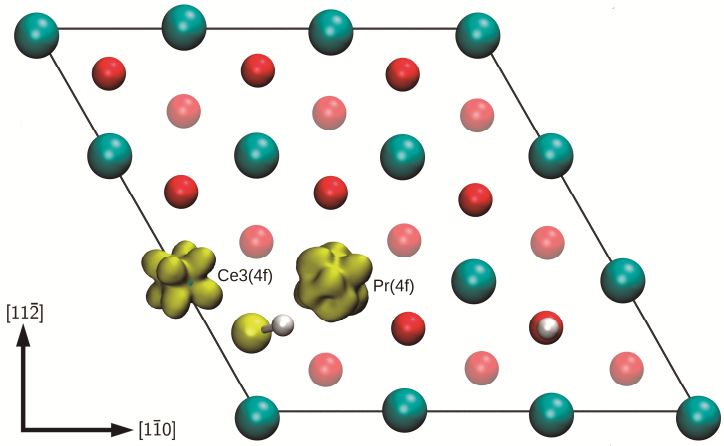

Figure 4: Electronic structure of the HS-H/$Ce_{0.963}Pr_{0.037}O_{2-x}$(111) system. Spin polarization at a 0.05 e $Å^{-3}$ isovalue for Ce3(4f) and Pr(4f) orbitals. Positive and negative values are indicatedin yellow and gray, respectively.

For completeness, we also calculated H_2S interactions on the CeO_{2-x}(111) surface with a vacancy of O1. The weak interaction of the molecule (ΔE_{ads} = –0.32 eV) suggests a physisorption. Besides, due to H_2S interaction on Ce3 cation one of the H–S bonds become elongated (d(H–S) = 1.48 Å). However, there was no cleavage of the molecule. In this regard, we emphasize that our results agree with previously reported DFT results indicating that H_2S interaction on the reduced CeO_{2-x}(111) surface is weak (ΔE_{ads} = –0.45 eV), and that it occurs via interaction between the sulfur atom of H_2S and the Ce atom nearest neighbor to the oxygen vacancy [38].

In summary, the DFT+U calculations performed in this work indicate that molecular adsorption of H_2S on both the stoichiometric and O-deficient undoped ceria (111) surface is unfavorable due to weak interactions between the H_2S molecule and the ceria surface. Moreover, this result agrees with previous reports of literature [33,38].

On the other hand, molecular adsorption of H_2S on the O-defective $Ce_{0.963}Pr_{0.037}O_{2-x}$(111) surface is an exothermic process. The molecular interaction of H_2S is followed by a dehydrogenation process: $H_2S \rightarrow SH + H$, which occurs over the O1-hole with almost no energy barrier. Furthermore, the electronic structure of the HS-H/$Ce_{0.963}Pr_{0.037}O_{2-x}$(111) system reveals that the H–SH bond was heterolytically broken into H^+ and HS^- species.

4. Conclusions

Our DFT+U calculations reveal a key role of Pr dopant during H_2S interactions on ceria surface. Although, molecular H_2S interactions on the undoped ceria surface are very weak, on the oxygen deficient $Ce_{0.963}Pr_{0.037}O_{2-x}$(111) surface the H_2S molecule easily dehydrogenates into HS^- and H^+ species. The HS^- fragment can bond to either reduced Pr^{3+} or Ce^{3+} cations, while the H^+ fragment bonds to the nearest lattice oxygen anion forming a surface hydroxyl. Our findings indicate that Pr dopant promotes the H_2S dehydrogenation process and, thus, can help to develop new ceria-based supports capable to effectively mitigate sulfur poisoning of the Ni metal active phase.

Acknowledgements

The authors acknowledge the Universidad de Buenos Aires (UBACyT-20020150100095BA) and ANPCyT (FONCYT-PICT-2011-1312) for their financial support.

References

[1] M. Balat. Int. J. Hydrogen Energy 2009, 34, 3589–603.

[2] C.P. Sigar, S.L. Soni, J. Mathur, D. Sharma. Energy Source A 2009, 31,139–48.

[3] E. Kirtay. Energy Conversion and Management 2011, 52, 1778–1789.

[4] L. Sánchez-Silva, D. López-González, A.M. Garcia-Minguillan, J.L. Valverde, Bioresource Technol. 2013, 130, 321–331.

[5] S. Chiu, C. Kao, M. Tsai, S. Ong, C. Chen, C.S. Lin. Bioresour. Technol. 2009, 100, 833 (1–8).

[6] W. Peng, Q. Wu, P. Tu, J. Appl. Phycology 2001,13, 5–12.

[7] L. Rodolfi, G. Zitelli, N. Bassi, G. Padovani, N. Biondi, G. Bonini, M. Tredici. Biotechnol. Bioeng. 2009, 102, 100 (1–12).

[8] P. Schenk, S. Thomas-Hall, E. Stephens, J. Mussgnug, C. Posten, O. Kruse, B. Hankamer. Bio-energy Res. 2008, 1, 20–43.

[9] J. Haase. J. Phys.: Condens. Matter 1997, 9, 3647.

[10] S.L. Lakhapatri, M.A. Abraham. Appl. Catal. A: Gen 2009, 364, 113–121.

[11] J.M. Thomas, W.J. Thomas. *Principles and Practice of Heterogeneous Catalysis*, in: VCH, New York (1997).

[12] Ch. Luo, W. Wang, M. Qiao, K. Fan. J. Molec. Catal. A: Chem 2002,184, 379–.

[13] C.H. Bartholomew, P.K. Agrawal, J.R. Katzer. Adv. Catal. 1982, 31, 135–242.

[14] R.M. Navarro, M.A. Peña, J.L.G. Fierro. Chem. Rev. 2007, 107, 3952–3991.

[15] A. McCoy, M.J. Duran, A-M. Azad, S. Chattopadhyay, M.A. Abraham. Energy & Fuels 2007, 21, 3513–3519.

[16] Z. Chafi, N. Ouafek, E. Boudjennad, N. Keghouche, C. Minot, Sciences & Technologie A 2010, 32, 15–20.

[17] F. Passos, E. de Oliveira, L. Mattos, F. Noronha. Catal. Today 2005, 101, 23–30.

[18] B. Milberg, A. Juan, B. Irigoyen. Appl. Surf. Sci. 2017, 401, 206–217.

[19] L. Eyring, *Handbook on the Physics and Chemistry of Rare Earths*, in: K.A. Gschneider, L. Eyring (Eds.), North-Holland, Amsterdam, 1979.

[20] J.C. Conesa, Surf. Sci. 1995, 339, 337–352.

[21] M. Nolan, S. Grigoleit, D.C. Sayle, S.C. Parker, G.W. Watson, Surf. Sci. 2005, 576, 217–229.

[22] N.V. Skorodumova, M. Baudin, K. Hermansson, Phys. Rev. B 2004, 69, 075401.

[23] G. Kresse, J. Furthmuller, Comput. Mater. Sci. 1996, 6, 15.

[24] G. Kresse, J. Hafner, J. Phys. Rev. B: Cond. Matt. Mat. Phys. 1993, 47, 558.

[25] H. Monkhorst, J. Pack, Phys. Rev. B 1976, 13, 5188–5192.

[26] M. Nolan, S. Grigoleit, D.C. Sayle, S.C. Parker, G.W. Watson, Surf. Sci. 576(2005) 217–229.

[27] H. Li, H. Wang, X. Gong, Y. Guo, Y. Guo, G. Lu, P. Hu, Phys. Rev. B 2009, 79, 193401 (1–4).

[28] C. Castleton, J. Kullgren, K. Hermansson, J. Chem. Phys 2007, 127, 244704 (1–11).

[29] Y. Tang, H. Zhang, L. Cui, C. Ouyang, S. Shi, W. Tang, H. Li, J. Lee, L. Chen, Phys.Rev. B 2010, 82, 125104 (1–9).

[30] R.F.W. Bader. Chem. Rev. 1991, 91 (5), 893–928.

[31] W. Tang, E. Sanville, G. Henkelman. J. Phys. Condens. Matter 2009, 21 (8), 84204.

[32] G. Henkelman, A. Arnaldsson, H. Jónsson, Comput. Mater. Sci. 2006, 36, 354–360.

[33] Hsin-Tsung Chen, YongMan Choi, Meilin Liu, M. C. Lin. J. Phys. Chem. C 2007, 111, 11117–11122.

[34] Y. Tang, H. Zhang, L. Cui, C. Ouyang, S. Shi, W. Tang, H. Li, J. Lee, L. Chen. Phys. Rev. B 82 (2010) 125104 (1–9).

[35] A. Hartridge, M.G. Krishna, A.K. Bhattacharya, Mater. Sci. Eng. B 57 (1999)173–178.

[36] N.V. Skorodumova, S.I. Simak, B.I. Lundqvist, I.A. Abrikosov, B. Johansson. Phys. Rev. Lett. 2002, 89, 166601 (1–4).

[37] Z.-Y. Pu, J.-Q. Lu, M.-F. Luo, Y.-L. Xie, J. Phys. Chem. C 2007, 111, 18695–18702.

[38] A.D. Mayernick, R.Li, K.M. Dooley, M.J. Janik. J. Phys. Chem. C 2011, 115, 24178–24188.

Journal of the Argentine Chemical Society

NICKEL DEPOSITION ON CERIA: A DFT+U STUDY

Dan Rajsfus[1], Agustín Salcedo[1,2], Brian Milberg[1,2], Beatriz Irigoyen[1,2*]

[1] *Universidad de Buenos Aires. Departamento de Ingeniería Química, Pabellón de Industrias, Ciudad Universitaria, (1428) Buenos Aires, Argentina.*

[2] *CONICET - Universidad de Buenos Aires. Instituto de Tecnologías del Hidrógeno y Energías Sostenibles (ITHES). Buenos Aires, Argentina.*

** Corresponding author. E-mail: beatriz@di.fcen.uba.ar*

Received February 25th, 2017. Accepted in final form May 10th, 2017

Abstract

In this work, we studied the deposition of nickel (Ni) particles and on the (111) surface of CeO_2 (ceria) within a DFT+U framework in order to gain a better understanding of the structural characteristics of Ni/CeO_2 catalysts at atomic level. We examined different geometrical configurations for Ni: isolated (hollow) and in clusters (pyramidal and rhomboidal). Our results show that, for these configurations, there is a strong interaction between Ni and the support, with a charge transference from Ni to ceria. In the case of the Ni_4 clusters, the computed adsorption energy indicates that the rhomboidal configuration is more stable than the pyramidal one. Besides, there is a charge delocalization in the hole between the Ni^{1+} and O^{2-} ions in both Ni_4 configurations.

Resumen

En este trabajo se estudió la deposición de partículas de níquel (Ni) sobre la superficie (111) del CeO_2 (ceria) efectuando cálculos mecano-cuánticos DFT+U, con el objetivo de mejorar la comprensión a nivel atómico de las características estructurales de los catalizadores Ni/CeO_2. Se analizaron diferentes configuraciones geométricas para el Ni: aislado (*hollow*) y formando clústeres (piramidal y romboidal). Nuestros resultados indican que para esas configuraciones existe una fuerte interacción entre la fase activa Ni y el soporte, computándose una transferencia de carga desde el Ni hacia el CeO_2. En cuanto a los clusteres Ni_4, los valores calculados de energía de adsorción indican que la disposición romboidal es más estable que la piramidal. Además, se observa una deslocalización de densidad electrónica en la cavidad entre los iones Ni^{1+} y los aniones O^{2-} en ambas configuraciones.

Palabras Clave: Deposición de níquel; Óxido de cerio; Clusters Ni4; Cálculos DFT+U

Keywords: Nickel deposition; Cerium oxide; Ni4 clusters; DFT+U calculations

1. Introduction

In the current global context, where the growing demand of energy motivates the search of unconventional alternatives, hydrogen could become the main renewable energy source in the future. Molecular hydrogen (H_2) stands out because it can be stored in both liquid and gaseous state, and distributed by pipes [1]. In the long term, H_2 could replace natural gas because it is an environmentally friendly combustible, with an attractive cost [2]. Because of this, different international institutions promote and support the development of new safe and competitive technologies for hydrogen production, in order to satisfy the energetic needs of the growing population [1].

Currently, 95% of the global H_2 production originates from hydrocarbons, while only 4% is obtained from water electrolysis and 1% from biomass. The H_2 production from hydrocarbons has carbon dioxide (CO_2) as a by-product, which is considered the main responsible of greenhouse effect. Right now, the focus is shifting to generating H_2 from primary energy sources as wind, biomass and solar energy, in order to gradually replace the traditional processes [3].

Also, considering that H_2 is mainly obtained from catalytic processes, the design of catalysts with low cost, high activity, and high selectivity is particularly important.

One of the main catalytic processes employed for the production of hydrogen is the Steam Methane Reforming (SMR). Currently, SMR is the most important on an industrial scale; not only for H_2 production but also for syngas (CO e H_2) one, which is widely used for the synthesis of methanol and ammonia [4].

A very important challenge in the design of catalysts for hydrogen production is replacing noble metals as Pt and Rh, with more accessible and economical alternatives that at the same time provide equivalent catalytic performance. Nickel is an abundant and economical transition metal, and is widely used in catalytic processes as alcohols and hydrocarbons reforming reactions. Even though Ni catalyst show a high initial activity, it is rapidly deactivated by carbon deposition [5]. Another factor that affect the performance of Ni is the presence of sulfur in the feed stream. This is because sulfur poisons the catalyst, even in concentrations on the order of parts per billion [6].

Reducible oxides can be used as supports for the metal active phase, as they can either directly participle in the reaction or change the chemical properties of the metal. Historically, alumina (Al_2O_3) was the most common support for Ni-based catalysts [7]. However, CeO_2 (ceria) is an alternative support for Ni of special interest due to its oxygen storage capacity (OSC), which has a key role in improving the resistance of Ni to coke deposition [8–10]. This feature is mainly

attributed to an easy oxygen donation, which is originated by the ability of Ce cation to change its formal oxidation state from Ce^{4+} to Ce^{3+} [11,12]. Besides, CeO_2 can substantially improve the stability and catalytic performance of Ni.

Ceria is commonly used in three-way catalysis (TWC), sulfur oxides removal, preferential oxidation of carbon monoxide (CO-PROX), water-gas shift reaction (WGS) and H_2 production from alcohols and hydrocarbons, among others [13,14].

Previous studies have shown that Ni/CeO_2 catalysts are active and selective for both water-gas shift and steam reforming reactions [15–17]. Despite this, studies at fundamental level of their structure and electronic properties are still scarce in the literature. Therefore, in the present work we present a detailed theoretical study of the Ni/CeO_2 system. This study involved density functional theory (DFT) calculations, that we performed with the Hubbard (U) correction for Ce(4f) orbitals. We examined the metal-support interactions, as well as the changes in geometrical structure and electronic properties of CeO_2 resulting from Ni deposition.

2. Theoretical Methods

Cerium oxide has a fluorite-type cubic structure, with a reported experimental value for its lattice parameter of 5.41 Å [18]. This structure consists of a face-centered cubic (fcc) system of Ce^{4+} cations, with O^{2-} anions filling the tetrahedral voids. We constructed the model of CeO_2 surface by cleaving the optimized bulk cell with the (111) plane and retained an extra oxygen layer. We choose the (111) surface to study Ni deposition because it is the most stable among the low-index (111), (110) and (100) surfaces, and corresponds to minimal Ce–O bonds cleavage [19–21]. Fig. 1 shows a front view of the clean CeO_2(111) surface, where 3 layers can be seen (surface oxygen, Ce and subsurface oxygen).

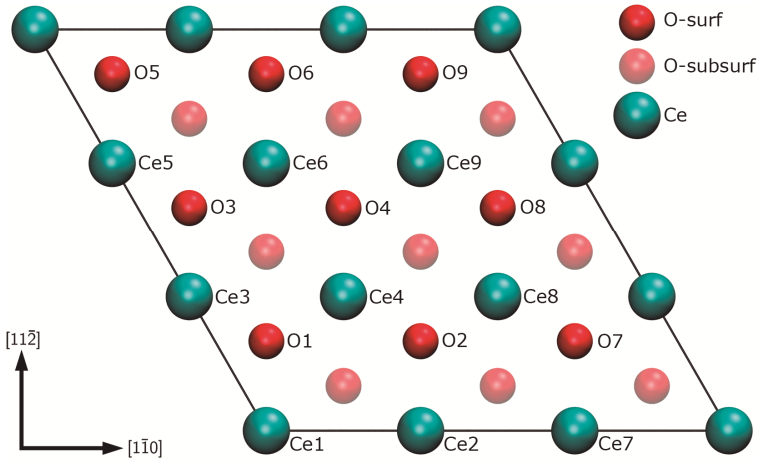

Figure 1. Front view of the CeO_2(111) slab.

First principles calculations were performed within the framework of density functional theory (DFT) as implemented in the Vienna Ab-initio Simulation Package (VASP) [22,23]. The Kohn-Sham equations were solved with the generalized gradient approximation (GGA), and the exchange correlation functional of Perdew-Burke-Ernzerhof (PBE). All calculations are spin-polarized. Geometries were optimized until the Hellmann-Feynman forces had converged to less than 0.02 eV/Å. The cutoff energy of the plane wave basis was set to 500 eV, and the core electrons were represented with the projector augmented wave (PAW) method. We used the Ce($5s^2$, $5p^6$, $6s^2$, $5d^1$, $4f^1$), Ni($3d^8$ $4s^2$) and O($2s^2$, $2p^4$) configurations for valence electrons.

Self-consistent calculations were performed sampling the Brillouin zone with a 3×3×1 k-points grid under the Monkhorst-Pack scheme [24].

The standard DFT formulation usually fails to describe strongly correlated electrons in partially occupied d and f orbitals, due to a deficient treatment of electron correlation. This limitation can be corrected to some extent by using the DFT + U method, where the introduction of a Hubbard 'U' parameter modifies the electron self-interaction error and enhances the description of the correlation effects. Therefore, the value U_{eff} = 5 eV was chosen for the Ce(4f) states as it correctly described the atomic and electronic structure of both CeO_2 and CeO_{2-x} systems [25,26].

Oxidation states and electron occupancy were computed by performing Bader charge and spin charge density analysis [27,28,29].

Nickel adsorption energy ($\Delta E_{ads,Ni}$) on the $CeO_2(111)$ surface was calculated as:

$$\Delta E_{ads,Ni} = E[Ni_y/CeO_2(111)] - E[Ni_y] - E[CeO_2(111)]$$

In this formula, $E[Ni_y/CeO_2(111)]$ represents the computed total energy of the different systems, $E[CeO_2(111)]$ is that of the clean ceria surface, and $E[Ni_y]$ is the corresponding total energy of Ni isolated species (y=1) or Ni_4 clusters in vacuum.

We also evaluated the charge density difference for the two cluster configurations. To make these plots, we calculated the charge density difference matrix (ρ_{diff}) as:

$$\rho_{diff} = \rho[Ni_4/CeO_2(111)] - \rho[Ni_4] - \rho[CeO_2(111)]$$

Here, $\rho[Ni_4/CeO_2(111)]$ is the charge density matrix for the optimized systems after relaxation. Then, we obtained $\rho[CeO_2(111)]$ by performing atomic fixed position calculations for the slab in the exact same post-relaxation geometrical configuration, but without the Ni_4 adsorbate. The opposite was done to obtain $\rho[Ni_4]$.

3. Results and Discussion

In this work, we studied the deposition of nickel particles on the $CeO_2(111)$ surface (Fig. 1). For an isolated single Ni atom, different adsorption sites can be explored, namely on-top of an O

anion, on the bridge between two O anions, or in the hollow position, where Ni atom adsorbs on a hollow site coordinated to three surface O anions. The later has been found to be the most stable configuration [17]. Nickel can also be deposited in small clusters. A Ni_4 three-dimensional pyramidal cluster is the most stable geometry in gas phase, closely followed by a planar rhombohedral structure [30,31]. We examined Ni deposition on a hollow site as well as both Ni_4 structures.

3.1. Ni Hollow

The interaction of an isolated Ni species on the $CeO_2(111)$ surface led to Ni adsorption on a hollow position. In our slab, the Ni atom was placed occupying the hole in the center of a triangle enclosed by O2, O4 y O8, as shown in Fig. 2. The computed adsorption energy for this configuration was $\Delta E_{ads,Ni}$ = -3.95 eV. The distance between Ni and the nearest neighbor O anions was 1.89 Å.

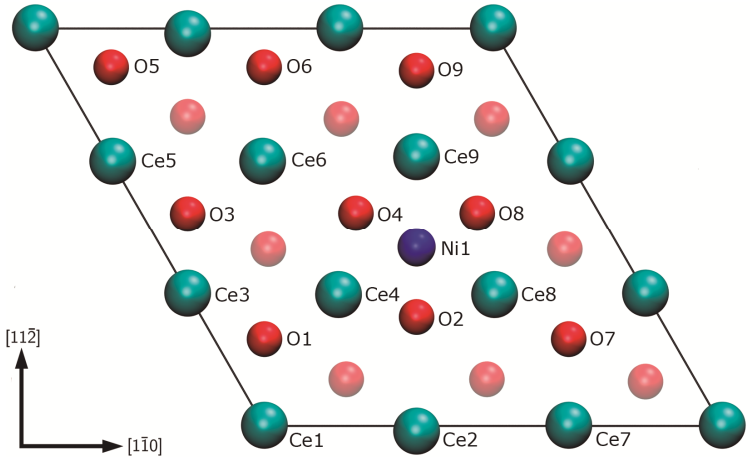

Figure 2. Front view of the $Ni_{Hollow}/CeO_2(111)$ slab

Bader charge analysis (see Table 1) indicated 8.9e for Ni, with a spin magnetization of 1.41 μB. Similar values of 8.9e and 1.2 μB where observed for Ni^{2+} ions in the NiO(100) surface [32]. Therefore, the Ni ion was characterized as Ni^{2+}.

When nickel becomes oxidized to Ni^{2+} due to its adsorption on a hollow site, two Ni(4s) electrons are transferred to the Ce(4f) band, leading to the reduction of two Ce cations. Accordingly, Bader charge analysis shows 9.9e for Ce5 and Ce6, with spin magnetizations of 1.0 μB, values corresponding to Ce^{3+} cations.

Our calculations indicate that an isolated Ni species adsorbs on the $CeO_2(111)$ surface as Ni^{2+}, and are in good agreement with the results of other theoretical and experimental works [15–17]. Particularly, our finding is consistent with that obtained from experimental measurements at low Ni coverages, which show that the electronic properties of Ni measured by Ni2p XPS and valence band UPS spectra are consistent with the formation of Ni^{2+} species [17].

Table 1. Bader charge and spin magnetization for selected ions.

System	Ion	Bader Charge (e)	Spin Magnetization (B)	Estimated Oxidation State
NiO (Ref. [32])	Ni	8.9	1.2	+2
Ni (bulk)	Ni	10.0	0.6	0
$Ni_{Hollow}/CeO_2(111)$	Ni	8.9	1.4	+2
	Ce5	9.9	1.0	+3
	Ce6	9.9	1.0	+3
	O2	7.2	0.2	-2
	O4	7.2	0.2	-2
	O8	7.2	0.2	-2
$Ni_{Pyr}/CeO_2(111)$	Ni1	9.7		+1
	Ni2	9.7		+1
	Ni3	9.7		+1
	Ni4	10.0	0.6	0
	Ce8	9.9	0.9	+3
	Ce9	9.9	0.9	+3
$Ni_{Rhom}/CeO_2(111)$	Ni1	9.7	1.0	+1
	Ni2	9.6	1.0	+1
	Ni3	9.6	1.0	+1
	Ni4	9.7	1.1	+1
	Ce1	9.8	-0.7	+3
	Ce2	9.8	-0.9	+3
	Ce8	9.9	-0.9	+3
	O1	7.2	0.1	-2
	O2	7.2	0.1	-2
	O3	7.2	0.1	-2
	O4	7.2	0.1	-2

3.2. Pyramidal Ni_4 cluster

Figure 3 shows the optimized geometrical configuration of the pyramidal Ni_4 cluster. The four Ni atoms are arranged in a pyramidal configuration with a Ni-Ni bond length of 2.30 Å, similar to the one reported in the literature for the cluster in vacuum [15]. The three Ni atoms closest to the surface form a triangle (Fig. 3) and are at 1.80 Å from O2, O4 and O8; while the other Ni atom locates in the center of this triangle, but considerably further from the surface. For this Ni_4 cluster in pyramidal structure, we computed an adsorption energy of -6.01 eV (-1.50 eV/Ni atom).

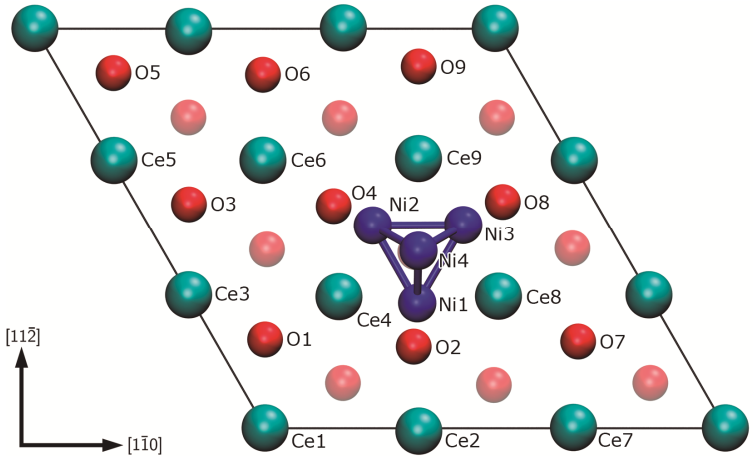

Figure 3. Front view of the $Ni_{Pyr}/CeO_2(111)$ slab

Bader charge analysis (Table 1) indicates 9.7e for Ni1, Ni2 and Ni3, which are the Ni ions closer to the surface. This value is higher than the 8.9e computed for Ni^{2+}, and comparable to that of 9.43e reported for Ni^{+1} in Ni-doped tetrahedrite [33]. So, this suggests that Ni1, Ni2 and Ni3 cations could be like Ni^{+1}. For Ni4, the upper nickel atom of the pyramid, Bader charge was instead computed in 10.0e. So, Ni4 can be considered as metallic Ni^0 atom. This configuration suggests that there is a weakening in the strength of the nickel–ceria interactions when Ni is not in direct contact with the oxide support.

On the other hand, when we examine the electronic configuration of Ce cations, only two of them (Ce8 and Ce9) are clearly reduced. In fact, the charge density difference plot shows some electronic charge is located in the hole between the Ni and the nearest O ions. This charge delocalization of Ni has been previously observed in the non-stoichiometric NiO(100) slab [33]. In this system, when an oxygen vacancy is generated in the NiO(111) surface, the electrons left behind are not localized neither on Ni nor on O. Instead, those electrons stay in the hole in between Ni and O ions.

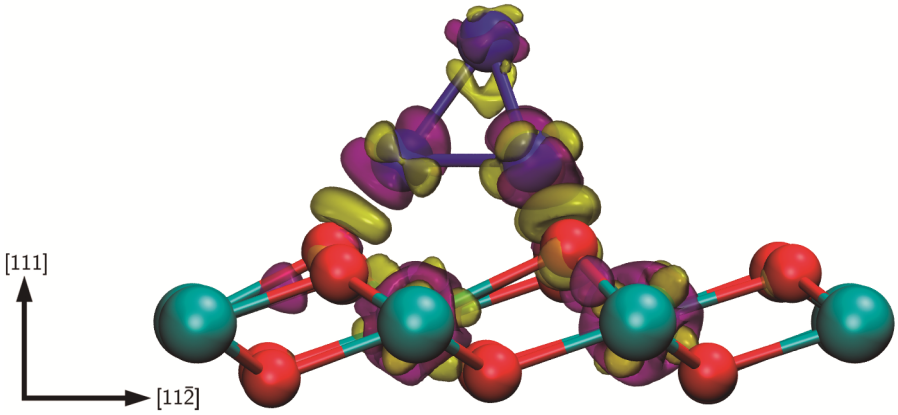

Figure 4. $Ni_{Pyr}/CeO_2(111)$. Charge density difference. The region of charge accumulation (isovalue +0.017) is presented in yellow, and that of electron depletion (isovalue −0.017) in purple.

3.3. Rhomboidal Ni_4 cluster

Figure 5 shows the optimized geometrical configuration of the rhomboidal Ni_4 cluster. In this case, the four Ni atoms are arranged in a rhomboidal structure on the ceria surface. The Ni-Ni bonds length was computed in 2.33 Å, similar to the 2.30 Å reported in other works [34]. The Ni atoms are lined up with O1, O2, O3 and O4, each of the 1.80 Å away from the nearest oxygen anion (see Fig. 5). For this configuration, we computed an adsorption energy of -6.44 eV (-1.61 eV for each Ni atom).

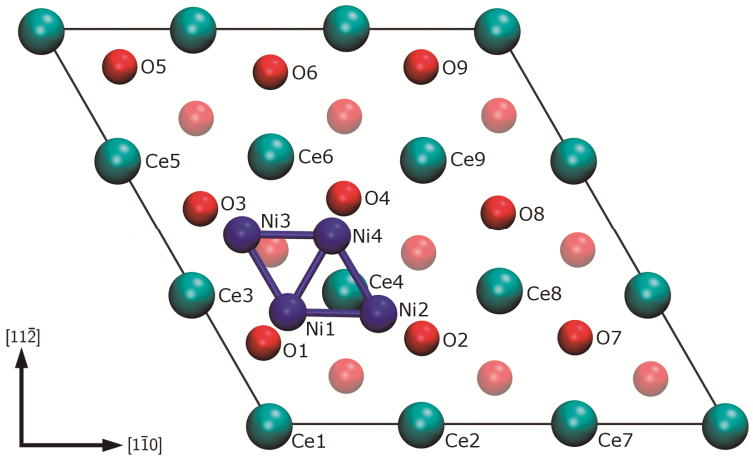

Figure 5. Front view of the $Ni_{Rhom}/CeO_2(111)$ slab.

Bader charge analysis indicates about 9.7e for all nickel ions, **comparable to that of** 9.43e reported for Ni^{+1} in Ni-doped tetrahedrite [33]. So, **this suggests that** the Ni cations **could be like** Ni^{+1}. This time we only can identify three Ce^{3+} cations (Ce1, Ce2 and Ce8), which Bader charge and spin magnetization values are reported in Table 1. The remaining electron density is located in the hole between the Ni ions and the surrounding O anions (Fig. 6), similar to what happened in the pyramidal cluster.

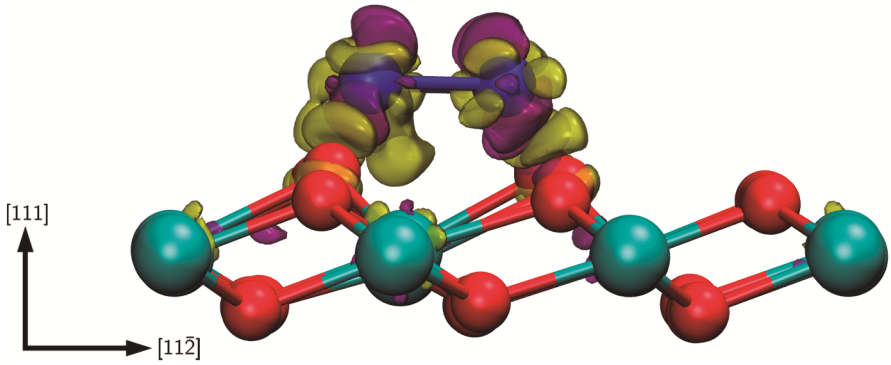

Figure 6. $Ni_{Rhom}/CeO_2(111)$. Charge density difference. The region of charge accumulation (isovalue +0.017) is presented in yellow, and that of electron depletion (isovalue −0.017) in purple.

4. Conclusions

Our DFT+U calculations have revealed strong interactions between the Ni active phase and the ceria surface, which modify the electronic properties of the ceria support and can drive the performance of Ni/CeO_2 catalysts. The interaction of an isolated Ni on the $CeO_2(111)$ surface (Ni adsorption on a hollow site) resulted in the formation of a Ni^{2+} and two Ce^{3+} species. Regarding the formation of Ni_4 clusters, the computed adsorption energy values indicate that the rhomboidal configuration is 0.43 eV more stable that the pyramidal one. Although both Ni_4 configurations show similar **Ni species**, in the pyramidal cluster the uppermost Ni atom is stabilized as Ni^0, suggesting that metal–oxide interactions are stronger for the first Ni layer. Besides, a noticeable delocalization of the charge density was observed in both Ni_4 clusters. The charge transferred by Ni oxidation is not completely localized on the Ce cations and, similarly to what was observed for the O-defective NiO(100) surface, some electron density remains in the hole between Ni and O anions. These findings provide better understanding of the $Ni\text{-}CeO_2$ interphase behavior and can help to advance the development of ceria-based supports for Ni active phase with improved catalytic performance.

Acknowledgements

The authors acknowledge the Universidad de Buenos Aires (UBACyT-20020150100095BA) and ANPCyT (FONCYT-PICT-2013-0573) for their financial support.

References

[1] J. N. Armor. Appl. Catal. A Gen. **1999**, 176 (2), 159-176.

[2] M. Balat, Int. J. Hydrogen Energy **2008**, 33, 4013-4029.

[3] H. Balat, E. Kirtay, Int. J. Hydrogen Energy **2010**, 35, 7416-7426.

[4] K. Sato, K. Fujimoto. Catal. Commun. **2007**, 8 (11), 1697-1701.

[5] B. C. Enger, R. Lødeng, J. Walmsley, A. Holmen. Appl. Catal. A Gen. **2010**, 383 (1–2), 119–127.

[6] A. Van Der Drift, J. Van Doorn, J. W. Vermeulen. Biomass and Bioenergy **2001**, 20 (1), 45–56.

[7] R. M. Navarro, M. A. Pena, J. L. G. Fierro, Chem. Rev. **2007**, 107, 3952-3991.

[8] A. Purnomo, S. Gallardo, L. Abella, C. Salim, H. Hinode, React. Kinet. Catal. Lett. **2008**, 95, 213-220.

[9] S. Xu, X. Yan, X. Wang, Fuel **2006**, 85, 2243-2247.

[10] F. B. Passos, E. R. De Oliveira, L. V. Mattos, F. B. Noronha, Catal. Today **2005**, 101, 23-30.

[11] Y. Zhou, J. Zhou. J. Phys. Chem. C **2012**, 116 (17), 9544–9549.

[12] Z. Chafi, N. Ouafek, E. Boudjennad, N. Keghouche, C. Minot, Sciences & Technologie A **2010**, 32, 15-20.

[13] D. García Pintos, Tesis doctoral: Estudio de materiales basados en óxidos de cerio usando cálculos mecano-cuánticos DFT, Facultad de Ingeniería, Universidad de Buenos Aires, **2014**.

[14] D. Xianjun, Z. Dengsong, S. Liyi, G. Ruihua, Z. Jianping, J. Phys. Chem. C **2012**, 116, 10009−10016.

[15] Y. Zhou, J. M. Perket, A. B. Crooks, J. Zhou. J. Phys. Chem. Lett. **2010**, 1 (9), 1447–1453.

[16] S. D. Senanayake, J. Evans, S. Agnoli, L. Barrio, T. L. Chen, J. Hrbek, J. A. Rodriguez. Top. Catal. **2011**, 54 (1–4), 34–41.

[17] J. Carrasco, L. Barrio, P. Liu, J. A. Rodriguez, M. V. Ganduglia-Pirovano. J. Phys. Chem. C **2013**, 117 (16), 8241–8250.

[18] L. Eyring, Handbook on the Physics and Chemistry of Rare Earths, in: K.A. Gschneider, L. Eyring (Eds.), North-Holland, Amsterdam, **1979**.

[19] J.C. Conesa, Surf. Sci. 1995, 339, 337–352.

[20] M. Nolan, S. Grigoleit, D.C. Sayle, S.C. Parker, G.W. Watson, Surf. Sci. **2005**, 576, 217–229.

[21] N.V. Skorodumova, M. Baudin, K. Hermansson, Phys. Rev. B **2004**, 69, 075401.

[22] G. Kresse, J. Furthmuller, Comp. Mat. Sci. **1996**, 6, 15.

[23] G. Kresse, J. Hafner, J. Phys. Rev. B: Cond. Matt. Mat. Phys. **1993**, 47, 558.

[24] H. Monkhorst, J. Pack, Phys. Rev. B **1976**, 13, 5188–5192.

[25] M. Nolan, S. C. Parker, G. W. Watson, Surf. Sci. **2005**, 595, 223-232.

[26] C. W. M. Castleton, J. Kullgren, K. Hermansson. J. Chem. Phys. **2007**, 127 (24).

[27] R. F. W. Bader. Chem. Rev. **1991**, 91 (5), 893-928.

[28] W. Tang, E. Sanville, G. Henkelman. J. Phys. Condens. Matter **2009**, 21 (8), 84204.

[29] G. Henkelman, A. Arnaldsson, H. Jónsson, Comput. Mater. Sci. **2006**, 36, 354-360.

[30] F. A. Reuse, S. N. Khanna. Chem. Phys. Lett. **1995**, 234 (1–3), 77–81.

[31] Q. L. Lu, Q. Q. Luo, L. L. Chen, J. G. Wan. Eur. Phys. J. D **2011**, 61 (2), 389–396.

[32] A. M. Ferrari, C. Pisani, F. Cinquini, L. Giordano, G. Pacchioni. J. Chem. Phys. **2007**, 127 (17), 174711.

[33] X. Lu, D. T. Morelli, Y. Xia, V. Ozolins. Chem. Mater. **2015**, 27 (2), 408–413.

[34] G. Schmid, Clusters and Colloids: From Theory to Applications, VCH, Weinheim, **1994**.